



# Morphogenesis of spin cycloids in a noncollinear antiferromagnet

Shashank Kumar Ojha<sup>a,b,1</sup>, Pratap Pal<sup>c</sup>, Sergei Prokhorenko<sup>d</sup>, Sajid Husain<sup>e,1</sup>, Maya Ramesh<sup>f</sup>, Xinyan Li<sup>a,b</sup>, Deokyoung Kang<sup>a,e</sup>, Peter Meisenheimer<sup>e</sup>, Darrell G. Schlom<sup>g,h</sup>, Paul Stevenson<sup>i,1</sup>, Lucas Caretta<sup>j</sup>, Yousra Nahas<sup>d</sup>, Yimo Han<sup>a,b</sup>, Lane W. Martin<sup>a,b,k,l</sup>, Laurent Bellaiche<sup>d,m</sup>, Chang-Beom Eom<sup>c</sup>, and Ramamoorthy Ramesh<sup>a,b,e,k,l,n,o,1</sup>

Affiliations are included on p. 7.

Contributed by Ramamoorthy Ramesh; received November 12, 2024; accepted March 21, 2025; reviewed by Sang Wook Cheong and Tsuyoshi Kimura

Pattern formation in spin systems with continuous-rotational symmetry (CRS) provides a powerful platform to study emergent complex magnetic phases and topological defects in condensed-matter physics. However, its understanding and correlation with unconventional magnetic order along with high-resolution nanoscale imaging are challenging. Here, we employ scanning nitrogen vacancy (NV) magnetometry to unveil the morphogenesis of spin cycloids at both the local and global scales within a single ferroelectric domain of (111)-oriented BiFeO<sub>3</sub>, which is a noncollinear antiferromagnet, resulting in formation of a glassy labyrinthine pattern. We find that the domains of locally oriented cycloids are interconnected by an array of topological defects and exhibit isotropic energy landscape predicted by first-principles calculations. We propose that the CRS of spin-cycloid propagation directions within the (111) drives the formation of the labyrinthine pattern and the associated topological defects such as antiferromagnetic skyrmions. Unexpectedly, reversing the as-grown ferroelectric polarization from  $[\bar{1}\bar{1}\bar{1}]$  to  $[111]$  produces a noncycloidal NV image contrast which could be attributed to either the emergence of a uniformly magnetized state or a reversal of the cycloid polarity. These findings highlight that (111)-oriented BiFeO<sub>3</sub> is not only important for studying the fascinating subject of pattern formation but could also be utilized as an ideal platform for integrating novel topological defects in the field of antiferromagnetic spintronics.

multiferroics | magnetoelectric | pattern formation | morphogenesis | spin cycloid

The emergence of self-organized spatiotemporal patterns in nonequilibrium and homogeneous open systems has long captivated scientists (1–5). These patterns, varying in complexity, manifest across a wide range of length scales—from spiraling galaxies to nanoscale Turing patterns in single layers of bismuth (6). In a quest to seek universality, extensive studies on a multitude of physical systems and mathematical models have led to the understanding that symmetry breaking and finite wavelength instabilities are key drivers of such pattern formation (2–4). In particular, since instabilities naturally arise near phase transitions, the study of pattern-forming systems has significantly advanced our understanding of phase transitions across various dimensions (3, 4, 7, 8).

Systems with continuous-rotational symmetry (CRS) in two dimensions (2D) (i.e., which remain invariant under any finite rotation within the plane) are particularly intriguing. In such systems, according to the topological connectivity of the motif, point, and line topological defects (regions of locally vanishing order parameters) often emerge as critical elements (9, 10). These defects play a crucial role in understanding the dynamics and evolution of patterns and lie at the core of understanding the disorganization of the ordered phase (7, 8). For instance, the melting of 2D crystals, as described by the Kosterlitz–Thouless–Halperin–Nelson–Young (KTHNY) theory (11–14), illustrates how various defects such as dislocations and disclinations play pivotal roles in phase transitions.

In the context of magnetism (15), these topological defects assume prime importance, as they give rise to nontrivial swirling spin textures (16) such as merons (half-skyrmions) and skyrmions that have shown promise for the realization of ultra-low-power electronics (17, 18). Such topological objects have been explored in various condensed-matter systems with broken space inversion symmetry, such as magnets, (17, 19) ferroelectrics/multiferroics, (20, 21) and chiral liquid crystals (22, 23). Although they have been stabilized in magnetic systems with CRS, their integration into magnetoelectric (ME) multiferroic systems remains relatively unexplored (24, 25). Owing to the inherent

## Significance

Lamellar systems with continuous rotational symmetry (CRS) provide an exciting avenue for exploring spatiotemporal pattern formation and the emergence of topological defects in nonequilibrium systems. In this study, we investigate these phenomena on the (111) easy magnetization plane of the room-temperature magnetoelectric multiferroic BiFeO<sub>3</sub>, known for its noncollinear spin texture. We uncover the emergence of glassy Labyrinthine spin texture of spin cycloids which hosts an array of isolated and hybrid topological defects. Notably, applying an electric field induces a noncycloidal nitrogen vacancy magnetometry contrast, which can be reconfigured by reversing the electric field polarity. These results reveal a unique manifestation of the magnetoelectric effect in spin systems with CRS.

Author contributions: S.K.O., P.P., C.-B.E., and R.R. designed research; S.K.O., P.P., S.H., M.R., X.L., D.K., D.G.S., L.C., Y.H., L.W.M., and C.-B.E. performed research; S.K.O., S.P., P.M., P.S., Y.N., L.B., and R.R. analyzed data; and S.K.O., S.P., S.H., and R.R. wrote the paper.

Reviewers: S.W.C., The State University of New Jersey; and T.K., University of Tokyo.

The authors declare no competing interest.

Copyright © 2025 the Author(s). Published by PNAS. This open access article is distributed under Creative Commons Attribution-NonCommercial-NoDerivatives License 4.0 (CC BY-NC-ND).

<sup>1</sup>To whom correspondence may be addressed. Email: so37@rice.edu, shusain@berkeley.edu, p.stevenson@northeastern.edu, or rramesh@berkeley.edu.

This article contains supporting information online at <https://www.pnas.org/lookup/suppl/doi:10.1073/pnas.2423298122/-/DCSupplemental>.

Published April 24, 2025.

ME coupling in such systems, local topological-spin textures could potentially be toggled with an external electric field, opening new possibilities for advanced applications in an electric-field-controlled antiferromagnetism (26). In this work, we demonstrate how CRS along with suitable electrostatic/geometrical boundary conditions could be used to tailor novel isolated and hybrid topological-spin textures in the multiferroic BiFeO<sub>3</sub>.

During the last two decades, BiFeO<sub>3</sub> has emerged as an exciting platform for the development of energy efficient, spin-based electronics (26–32). At room temperature, BiFeO<sub>3</sub> has a noncentrosymmetric distorted rhombohedral structure (33) (consisting of two corner shared pseudocubic unit cells) and exhibits a large spontaneous ferroelectric polarization  $\mathbf{P} \simeq 100 \mu\text{C}/\text{cm}^2$  which can point along any of the  $\langle 111 \rangle$  (hereafter, all crystallographic directions/planes are described in the pseudocubic notation) (*SI Appendix, Fig. S1*). The magnetic structure can be approximated to be a G-type antiferromagnet. The presence of the antisymmetric Dzyaloshinskii–Moriya interaction (DMI), however, leads to a small canting that further couples to the polarization to yield a long period ( $\sim 62 \text{ nm}$ ) cycloid (34–36) which rotates in a plane containing  $\mathbf{P}$  and  $\mathbf{k}$ , where  $\mathbf{k}$  points along a  $\langle 110 \rangle$  and is perpendicular to  $\mathbf{P}$  (37). The cycloid is accompanied by a spin-density wave perpendicular to the cycloidal plane (*SI Appendix, Fig. S1*).

In the bulk, for each direction of  $\mathbf{P}$ , symmetry conditions allow for only six propagation vectors “ $\mathbf{k}$ ” related through  $\pi/3$  rotations and corresponding to three antiferromagnetic domains (38). At the same time, recent first-principles calculations (39) indicate that such six-fold anisotropy could be negligible at the length scale of the cycloidal modulation. Particularly, reconstructing the ab initio calculated energy surface of antiferromagnetic spin cycloids in monodomain BiFeO<sub>3</sub> (Fig. 1A) reveals that the cycloid propagation directions contained in the (111) are energetically degenerate (*Materials and Methods*).

In this context, a critical question emerges: What is the expected spatial pattern of the cycloids on the (111) surface of BiFeO<sub>3</sub>? A common intuition suggests that the degeneracy in orientational order, imposed by the CRS of spin cycloids, would lead to the continuous rotation of cycloids within the (111) plane (Fig. 1B). Additionally, regions with different local orientational order (40) could interact and compete, potentially giving rise to topological defects such as disclinations and dislocations (discussed later). This makes (111)-oriented BiFeO<sub>3</sub> a rich platform for exploring complex and nontrivial spin textures. In this article, by using high-resolution nitrogen-vacancy (NV) diamond-based scanning probe microscopy, we demonstrate how the CRS imposed on the pseudocubic (111) surface of BiFeO<sub>3</sub> leads to the complete morphogenesis of the spin structure, resulting in a glassy labyrinthine pattern (41). This pattern features a diverse range of isolated and hybrid topological defects, emphasizing the intricate interplay between symmetry and topological defect formation. Interestingly, electrical switching of the as-grown  $\mathbf{P}$  direction from  $[\bar{1}\bar{1}\bar{1}]$  to  $[111]$  eliminates the labyrinthine patterns, resulting in a noncycloidal NV contrast which could be associated to either emergence of uniformly magnetized state or switching of the cycloid polarity.

It is emphasized that having a single ferroelectric domain is crucial for this study as the presence of multiple ferroelectric domains and their associated boundaries would introduce additional boundary conditions, thereby violating the requirement of CRS. In this spirit, single domain BiFeO<sub>3</sub> films were grown on SrRuO<sub>3</sub>-buffered SrTiO<sub>3</sub> (111) substrates as a model system (*Materials and Methods* and *SI Appendix, Fig. S2*). In this configuration, the rhombohedral distortion axis of BiFeO<sub>3</sub> aligns with the normal direction  $[111]$  of the SrTiO<sub>3</sub> substrate, leading to the stabilization of a single ferroelectric/ferroelastic domain (42) (*SI Appendix, Fig. S2*). The metallic SrRuO<sub>3</sub> bottom electrode effectively screens the depolarizing field in the BiFeO<sub>3</sub>

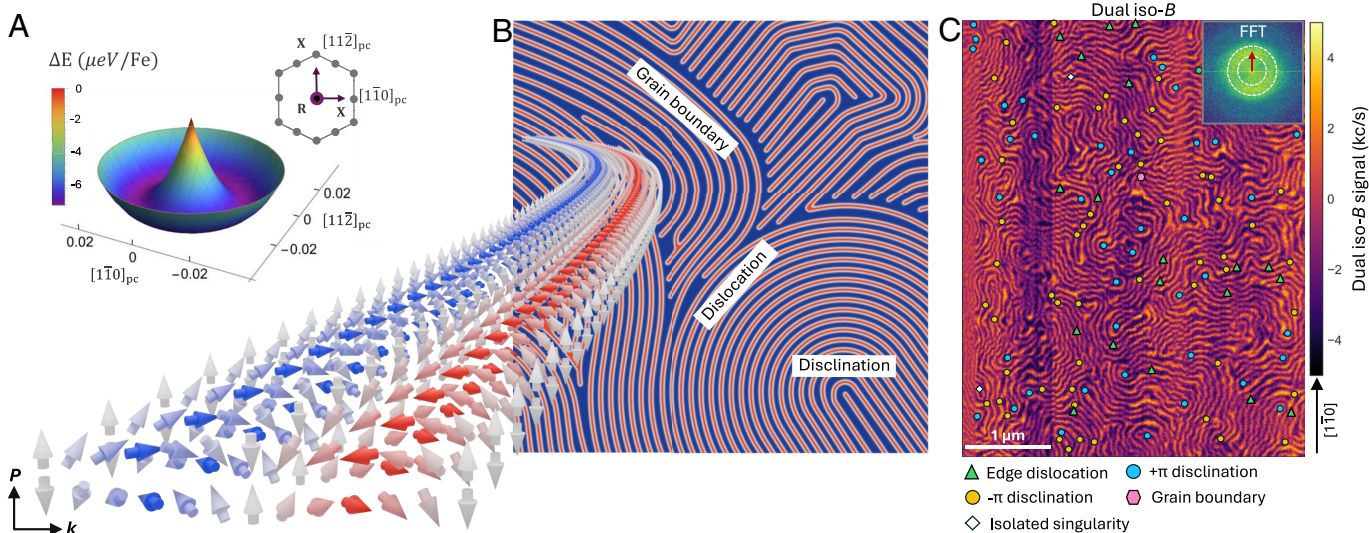


**Fig. 1.** Continuous-rotational symmetry and morphogenesis of spin cycloids. (A) Dependence of the spin cycloid energy on the propagation vector within the (111) calculated using the ab initio based Hamiltonian (39). The horizontal axes represent the  $[1\bar{1}0]$  and  $[11\bar{2}]$  orthogonal projections of the cycloid propagation vector centered on the  $R$  point of the pseudocubic Brillouin zone (BZ), as shown in the *Inset*. The *Inset* shows the corresponding (111) BZ cross-section with high symmetry  $X$  and  $R$  points indicated by gray and purple circles, respectively. (B) A schematic to show the continuous rotation of spin cycloids (red and blue stripes) in (111) of BiFeO<sub>3</sub>. When regions with different local orientational order meet, defects such as disclinations, edge-dislocations, and grain boundaries are formed. The actual spatial variation of spins for a curly stripe is shown projecting outward from the panel (B). As discussed, spins form a cycloid in the  $P$ - $k$  plane which is further modulated by an out-of-plane (perpendicular to  $P$ - $k$  plane) tilting due to DM interaction (for more details, see *SI Appendix, Fig. S1*). Here, two cycloids correspond to two antiparallel neighbors of Fe sublattice. (C) Magnetic contrast obtained in dual iso-B mode on a 600 nm  $[111]$  oriented BiFeO<sub>3</sub>. Various types of topological defects have been marked with different symbols listed at the *Bottom*. Fast Fourier transform of a  $4 \mu\text{m} \times 4 \mu\text{m}$  section (from *Bottom*) of the image is shown in the *Inset*. Spread in the  $\mathbf{k}$  vectors is shown with two concentric dotted white circles. A vertical red arrow shows the average  $\mathbf{k}$ . This also represents the equiax plane for  $\mathbf{k}$ -vector in the (111) plane.

film, thereby enforcing the  $\mathbf{P}$  vector to point completely into the film plane (specifically along the  $[\bar{1}\bar{1}\bar{1}]$  in as-grown state) resulting in the formation of a single ferroelectric domain (42) (*SI Appendix, Fig. S3*).

## Results

**Real-Space Imaging of Spin Cycloids.** In order to study the nature of the spin cycloids on the (111) surface of BiFeO<sub>3</sub>, we employed high-resolution nitrogen-vacancy diamond-based scanning probe microscopy (*SI Appendix, Fig. S4 and Materials and Methods*) (43, 44). Fig. 1C shows one representative dual iso- $B$  plot for a 600-nm-thick BiFeO<sub>3</sub> film. As is evident, both the spin-up and spin-down stripes that meander within the (111) of BiFeO<sub>3</sub> form percolating networks and give rise to a glassy labyrinthine pattern (41) (additional data, *SI Appendix, Fig. S4*). This observation contrasts with bulk BiFeO<sub>3</sub>, where symmetry constraints allow only six propagation vectors  $\mathbf{k}$ , related by  $\pi/3$  rotations, corresponding to three distinct antiferromagnetic domains (38). We attribute this difference to the presence of inhomogeneous strain in our samples (*SI Appendix, Fig. S5*), which effectively smears out the anisotropic energy landscape that governs cycloid propagation in bulk BiFeO<sub>3</sub>. As a result, the (111) orientation in our case behaves as if it were “isotropic” in the (111). This glassy behavior aligns qualitatively with our theoretical calculations (Fig. 1A), which show that the long-wavelength cycloidal modulations of the G-AFM BiFeO<sub>3</sub> state are energetically very close to being degenerate for propagation vectors confined within the (111) plane. Such a pattern has previously been observed in ferroelectrics and is generally regarded as an intermediate stage between the ordered and disordered phases, resulting from competing interactions (45–47). As discussed earlier, the formation of any pattern has

its roots in a finite wavelength instability of the homogeneous state. In multiferroic systems, this instability is often driven by long-range dipole–dipole interactions or the antisymmetric DMI (48). The fast Fourier transform (FFT) (*Inset, Fig. 1C*) of the dual iso- $B$  image appears isotropic and reveals an average wavelength of  $\sim 68$  nm, close to the cycloid periodicity in the bulk of BiFeO<sub>3</sub> (37). This observation implies that the formation of such a labyrinthine is connected to the well-known spin-cycloid instability in BiFeO<sub>3</sub> (37). We also emphasize that, while the isotropic FFT clearly demonstrates that our system broadly demonstrates CRS, this symmetry is not preserved in real space over large length scales, as the labyrinthine pattern does not remain invariant under continuous rotation by a finite angle. We attribute this to the sample growth process, where cooling from the high growth temperature to below the Néel temperature leads to local nucleation of the magnetic order parameter, resulting in regions with distinct local orientational orders. Nonetheless, CRS in real space is evident from the continuous rotation of spin cycloids (at mesoscale) within the (111) plane, accommodating all possible propagation vectors within the (111) of BiFeO<sub>3</sub> (*SI Appendix, Fig. S6*). Since the dual iso- $B$  data is semiquantitative, to validate our observation, we have also recorded measurements in full- $B$  mode (Fig. 2A). As seen, cycloid-propagation directions indeed continuously rotate within the (111), thereby validating our observation of a labyrinthine pattern (*SI Appendix, Fig. S7* for additional full- $B$  data). Interestingly, we also found that, unlike the case of (001), the stray field in (111) oriented films can not be solely attributed to the spin density wave (see *SI Appendix, section S2* for more details).

Further, apart from the isotropic nature of the FFT (as expected for a labyrinthine pattern), there is also a sparsing nature of the cycloid width (*Inset, Fig. 1C, dotted white circles*). This would mean that the periodicity of the cycloids has a distribution

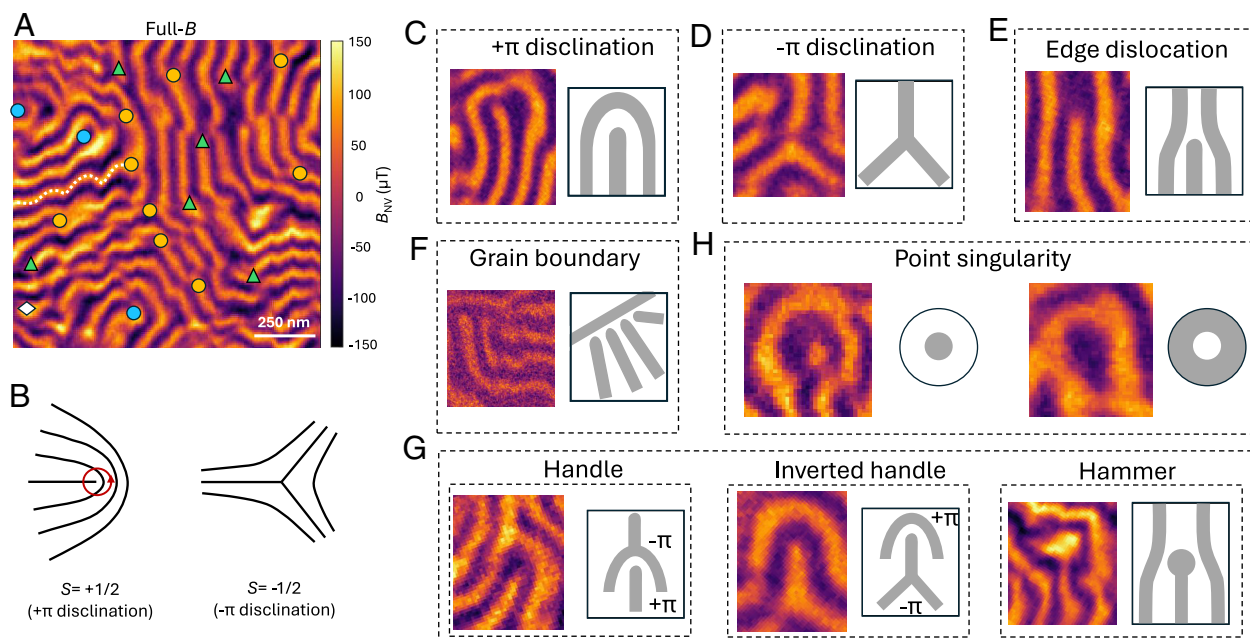


**Fig. 2.** Taxonomy of topological defects and interactions among them. (A) Magnetic contrast obtained in full- $B$  mode on a 300 nm thick (111) BiFeO<sub>3</sub> sample. A white dashed wavy line is used to highlight the oscillatory pattern in cycloids. Symbols are used to mark different topological defects. (B) Schematics to show the formation of two types of elementary line defects in planar systems with CRS. *Left* schematic shows the formation of  $+\pi$  disclination. Here, the angle  $\pi$  comes from the total angle covered by the director field when one encircles around the line defect in anticlockwise direction (shown with red circle). This leads to a winding number  $S = +1/2$  and  $-1/2$  (*Right* schematic) for  $+\pi$  and  $-\pi$  disclinations respectively. (C–F) General class of topological defects observed in homogeneous 2D systems with CRS. (G) Handle, inverted handle, and hammer like structure. (H) Isolated point singularity for both spin up (*Left* panel) and down (*Right* panel). Here, all the images have been taken from dual iso- $B$  scans on samples with thickness 300 nm, 600 nm, and 1,000 nm.

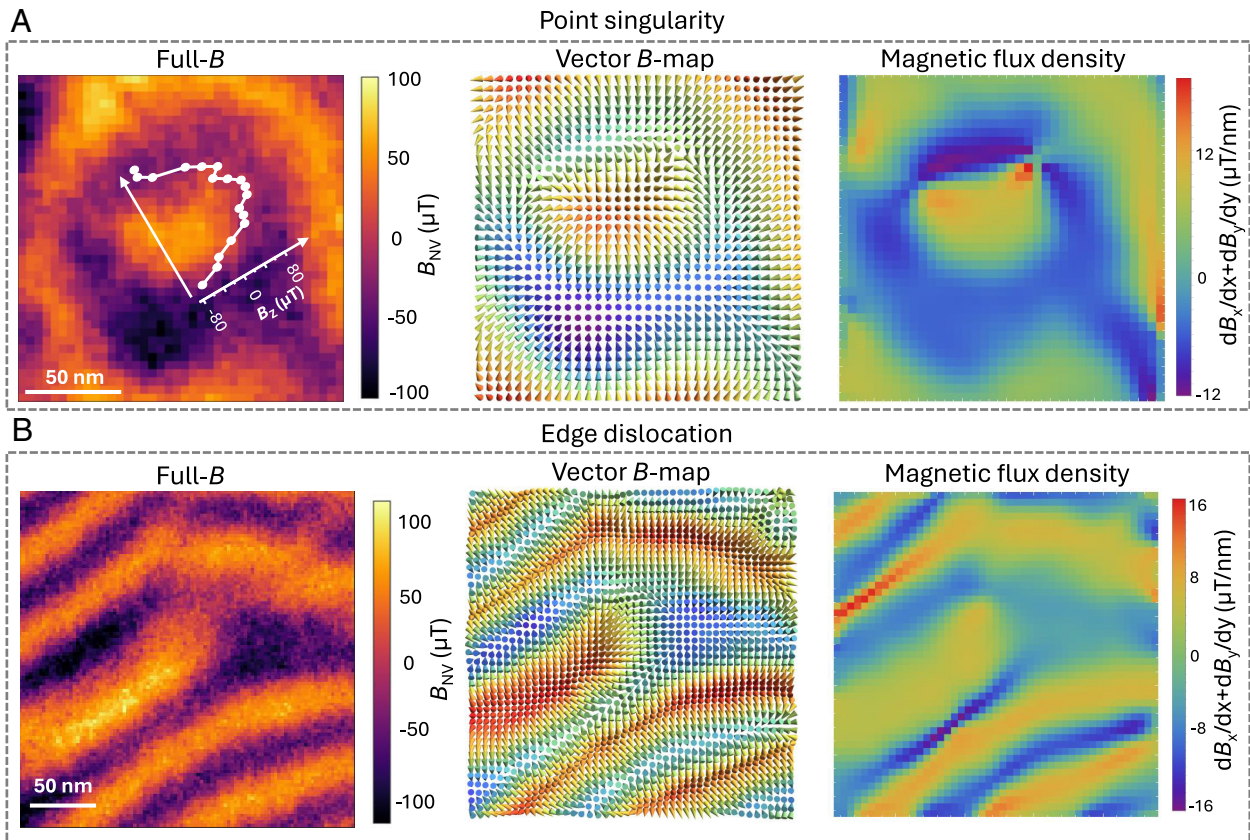


**Fig. 3.** Nature of spin texture around topological defects. (A) (Left panel) Full- $B$  image taken around a point singularity. In-set graph shows the line scan of  $z$ -component of the stray field across the singularity. The corresponding vector map of the normalized  $B$ -field and magnetic flux density has been shown in Middle and Right panels respectively. (B) (Left panel) Full- $B$  image taken around an edge dislocation. The corresponding vector map of the normalized  $B$ -field and magnetic flux density is shown in Middle and Right panels respectively. See *SI Appendix*, Figs. S11 and S12 for additional data.

spanning across all directions within the (111) (*SI Appendix*, Figs. S8–S10). We also found that the modulus of the  $B$ -field also varies randomly across cycloids (*SI Appendix*, Fig. S9). Since the magnitude of the canted moment is directly linked to the cycloid periodicity and the strength of the local  $B$ -field (49), these observations strongly indicate that spin cycloids have undergone subtle changes even at the unit-cell level. This observation may be attributed to the coexistence of instabilities in both the spatial and temporal domains (3). In the context of reaction–diffusion systems, it has previously been noted that instabilities in the temporal domain, such as a Hopf instability, could lead to oscillating patterns (50–52). When these temporal instabilities interact with spatial instabilities, such as a Turing or cycloidal instability (1), complex patterns could emerge with variations even at local scales. In particular, the presence of aperiodic modulations perpendicular to the cycloid propagation within the samples (dotted white line, Fig. 2A) suggest that a similar interplay of instabilities is relevant to this system.

**Topological Defects.** In systems with CRS, the local director field, which describes the direction and degree of orientational order, exhibits infinite degeneracy and therefore can align in any direction within a planar geometry. This leads to the formation of topological-line defects due to competing nature of local orientational order. The two most elementary topological defects,  $\pm\pi$  disclinations, which are characterized by winding numbers  $S = \pm 1/2$ , are illustrated (Fig. 2B). To explore these in the present case, we have mapped out the discontinuities in local cycloidal order across several samples (Fig. 1C and *SI Appendix*, Fig. S4)

and found a dense distribution of such disclinations. We have also identified a variety of hybrid-topological defects (identified by different symbols, Figs. 1C and 2A). A catalog of the same is presented in panels (C–G) in Fig. 2.

The observed elementary defects can be readily understood using homotopy-theory arguments (9). The  $\pm\pi$  disclinations (Fig. 2C and D) as well as edge dislocations (Fig. 2E) are a consequence of the spin-cycloid order parameter space which encompasses two planar rotational symmetries. The first symmetry is related to the continuous rotation of the cycloid-propagation vector within the (111) (Fig. 1A) and gives rise to disclinations (9) (Fig. 2C and D). The second rotational symmetry shifts the phase of harmonic-cycloid modulation along a given propagation vector and is responsible for the appearance of edge dislocations (53).

One particularly interesting aspect of such elementary-topological defects is that they possess a nonzero topological charge (attached to their topology) and can interact with each other (45, 54–56). We observed several hybrid defects arising from such interactions. For example, arrays of disclinations result in grain boundaries (Fig. 2F) while the interaction between  $\pm\pi$  disclinations leads to the formation of structures such as handle structures (Fig. 2G) (45). Additionally, a point defect can interact with an edge dislocation to form a hammer-like structure.

Beyond such elementary and hybrid defects, isolated point singularities are also identified (Fig. 2H). It is hypothesized that the cycloidal order initially forms locally before expanding across the sample—a phenomenon frequently observed in reaction–diffusion systems (1), which serve as models for pattern formation (10), and have also been applied to antiferromagnets (48, 57, 58). These

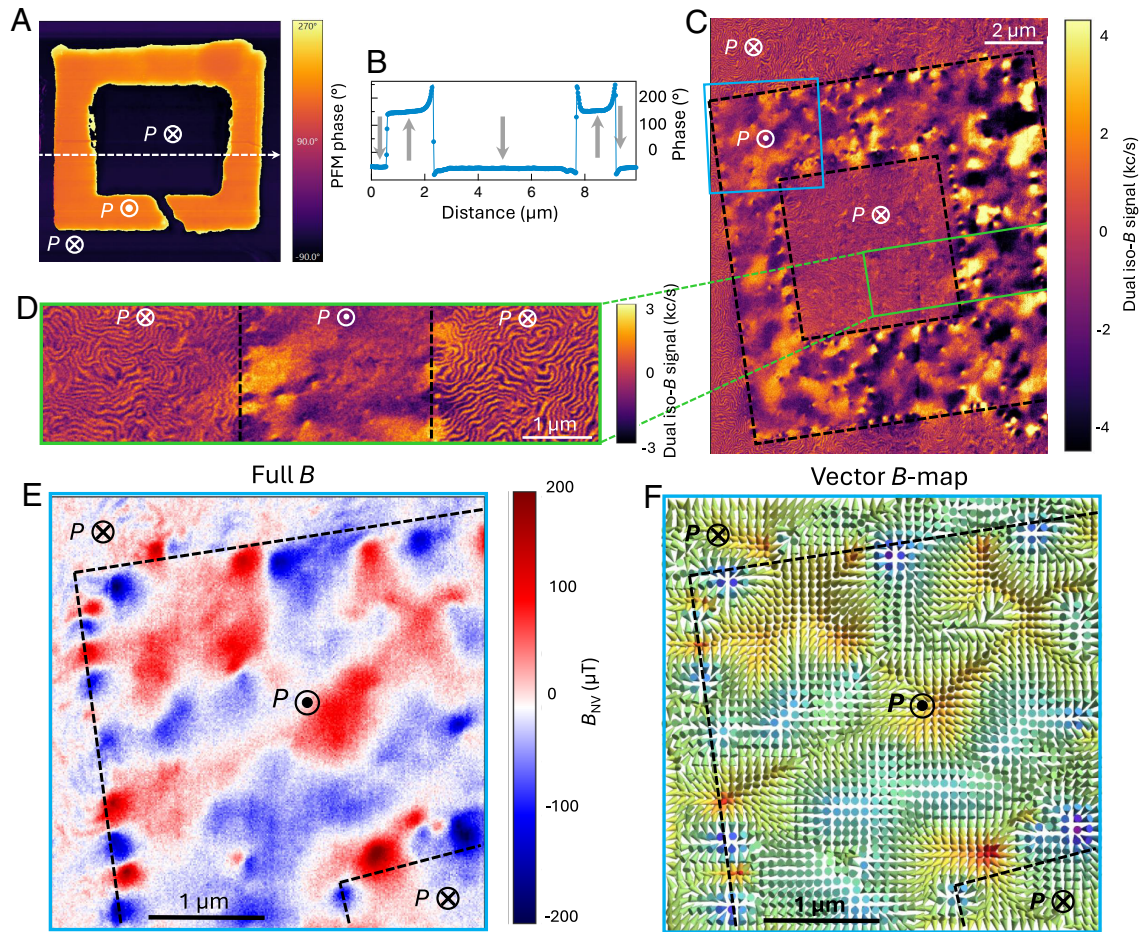


**Fig. 4.** Electric field switching. (A) Piezo-force microscopy (PFM) phase image of a box-in-box pattern switched with a conductive AFM tip on a 1,000 nm BiFeO<sub>3</sub>/SrRuO<sub>3</sub>/SrTiO<sub>3</sub> (111) sample. To create this box-in-box switched structure, first an 8 μm × 8 μm region was switched with -40V and then a 5 μm × 5 μm region was switched back with +40V. For as-grown films, the *P* vector points into the substrate along [111]. Upon application of a -40V, the polarization switches by 180 degree which can be again switched back to original by reversing the voltage to +40V. (B) The PFM phase along a horizontal line through the box-in-box pattern (see *SI Appendix, Fig. S3* for more details). (C) Corresponding dual iso-*B* image of box-in-box pattern written by PFM. Black dotted lines denote the switched boxes. Blue and green boxes denote two regions where high-resolution dual iso-*B* and full-*B* images were taken, presented in panels (D and E) respectively. Vector map of the normalized *B*-field for panel (E) has been shown in panel (F). Unnormalized vector *B* map is shown in *SI Appendix, Fig. S14*. Also, see *SI Appendix, Fig. S13* for *x*, *y*, and *z* components of *B*-field used to construct vector *B* map shown in the panel (E). Additional dataset on upward poled region on another sample is shown in *SI Appendix, Fig. S15*.

singularities are particularly intriguing, as they have the potential to host antiferromagnetic skyrmion-like spin textures. In the present case, they can be visualized by considering the complete winding of spins along the propagation of the underlying spin cycloids, fully modulated by the rotational symmetry in the (111) of BiFeO<sub>3</sub>. We note that, while ferroelectric solitons (i.e. topologically protected textures) have been crafted in epitaxial superlattices of the form SrTiO<sub>3</sub>/BiFeO<sub>3</sub>/SrTiO<sub>3</sub> (21), their observation in magnetic counterparts remains unexplored. To investigate this, we constructed a vector map of the local *B*-field around the singularity and found continuous rotation of the *B* field as expected for a skyrmion (Fig. 3A). Since there is no direct one-to-one mapping between the *B*-field and the actual spin texture, we focus on only the *z* component (*B<sub>Z</sub>*), which fully preserves the rotational symmetries of the out-of-plane magnetization (59). We find that its variation across the singularity (*Inset, Left* panel of Fig. 3A) closely resembles the *B<sub>Z</sub>* profile around the skyrmions previously reported in magnetic multilayer systems through NV magnetometry (59). In a recent theoretical calculation for BiFeO<sub>3</sub>, it is suggested that spin winding generates an extra polarization in response to the spin-current model:  $P_{ME} \approx e_{ij} \times (S_i \times S_j)$  parallel to the polarization

along the [111], thereby stabilizing the skyrmion in 3D (48). While the evolution of the local *B*-field in the present case strongly attests to the presence of a skyrmion-like spin texture, at least in 2D on the (111) surface, further investigation is needed to fully understand its structure in 3D. Inspired by this, we have also constructed the *B*-field vector map around an edge dislocation (Fig. 3B) and found that the evolution of the *B*-field is qualitatively consistent with that of a meron (spin texture equivalent to half of a skyrmion). These observations emphasize the potential of the (111) surface of BiFeO<sub>3</sub> for integrating novel spin textures and their electrical manipulation.

**Electric-Field Switching.** Our initial premise from the data (Figs. 1–3) was that such glassy labyrinthine patterns arise as a consequence of competing interactions during the emergence of the cycloid structure upon cooling from the synthesis temperature. We, therefore, hypothesized that electrical switching of the ferroelectric order in local regions could possibly provide a pathway to increase the degree of order in the cycloid (effectively “electrical annealing”) and perhaps could even lead to a perfectly hexagonally ordered cycloid lattice (38). In turn, bipolar electric-field switching of the ferroelectric state was carried out using

piezoresponse force microscopy (PFM) (*Materials and Methods* and Fig. 4A) to locally switch the BiFeO<sub>3</sub> layer (in a box-in-box pattern) as well as switching through a platinum top electrode in a metal–ferroelectric–metal capacitor structure (*SI Appendix, Fig. S16*). Fig. 4A illustrates the switching of the polarization (which, in the as-grown state, is along  $[\bar{1}\bar{1}\bar{1}]$ , i.e., toward the bottom SRO electrode) to point along  $[111]$ , as evidenced by the change in the phase of the piezoresponse signal by 180° (Fig. 4B). We were surprised to find that the first switching event (from the down- to up-poled state) led to the destruction of the cycloid state at the surface and the emergence of a noncycloidal NV image contrast. Switching back (from the up- to down-poled state) led to the re-emergence of the cycloid state. This deterministic switching is captured in the dual iso-*B* image which is qualitatively related to the *B*-field emerging from the sample (Fig. 4C), and a higher resolution/magnification image is also provided (Fig. 4D) along with the full-*B* map from a portion of this doubly switched region (Fig. 4E) with the corresponding vector *B* map (Fig. 4F). The effective *x*, *y*, and *z* components of the *B*-field distribution in the up-poled region do not display the cycloid-based labyrinthine pattern either (*SI Appendix, Fig. S13*). The fundamental origins of such an NV image contrast are still unclear; however, it is hypothesized that it may be either related to flexoelectric/flexomagnetic effects in BiFeO<sub>3</sub>, as has been illustrated previously (60, 61) or to switching of cycloid polarity (*SI Appendix, section S2 and Figs. S18–S23*). If the contrast is interpreted as a noncycloidal phase, such a uniform, canted moment structure in BiFeO<sub>3</sub> has been theoretically predicted to be an altermagnet (62, 63) which is being investigated as a future research problem.

## Conclusions and Outlook

In summary, we have elucidated how the CRS of cycloid propagation in the (111) drives the comprehensive spatial organization of the spin cycloid, culminating in a diverse spectrum of isolated- and hybrid-topological defects which carry substantial implications for the advancement of polar antiferromagnets. Unexpectedly, we observe that switching of the polarization in such a single domain (111)-oriented BiFeO<sub>3</sub> leads to the unwinding of the cycloid into a noncycloidal, uniformly magnetized state over a micron length scale. Future work will be directed toward a complete understanding of the “noncycloidal” magnetic contrast using XMCD-PEEM to image a ferromagnet that is deposited onto this switched state, as well as systematic, temperature-dependent studies to delve deeper into the topological defects. Recent breakthroughs in nonlocal transport on BiFeO<sub>3</sub> have highlighted the critical role of the spin cycloid in the conceptualization and realization of magnonic devices (32). We believe that our identification of various spatiotemporal instabilities presents key insights that could inform the development of an exhaustive pattern-forming model for BiFeO<sub>3</sub>. A detailed understanding of these instabilities will be instrumental in the meticulous tuning of material growth parameters, essential for the creation of a perfect macroscopic 1D spin channel which would open new avenues for electrical controlled antiferromagnetic spintronics.

## Materials and Methods

**Sample Growth.** (111) monodomain (single ferroelastic and ferroelectric) BiFeO<sub>3</sub> thin films were grown on cubic SrTiO<sub>3</sub> (111) substrate, buffered by a thin SrRuO<sub>3</sub> (~25 nm) layer, by RF magnetron sputtering. First, a ~25 nm thick

SrRuO<sub>3</sub> bottom electrode layer is deposited by 90°-off-axis sputtering at 600 °C which is followed by a growth of 300 nm to 1,000 nm BiFeO<sub>3</sub> films by double-gun off-axis sputtering at 750 °C with Ar:O<sub>2</sub> ratio of 4:1 at a total pressure of 400 mTorr (64). The SrRuO<sub>3</sub> layer serves three key functions: First, it acts as a bottom or ground electrode for out-of-plane device measurements; second, it generates a depolarization field that aligns the polarization of the BiFeO<sub>3</sub> downward; and third, it serves as a buffer layer to accommodate the large lattice mismatch between the BiFeO<sub>3</sub> and the substrate (65). The BiFeO<sub>3</sub> target used contains 5% excess Bi<sub>2</sub>O<sub>3</sub> to compensate for bismuth volatility during thin film deposition. Before growth, SrTiO<sub>3</sub> (111) was first etched for 30 seconds in buffered-hydrofluoric acid and then treated at 900 °C for 6 h under 30 sccm oxygen gas flow. The 100 nm thick BiFeO<sub>3</sub> (001)-oriented samples were grown on TbScO<sub>3</sub> substrates via reactive molecular-beam epitaxy in a VEECO GEN10 system, using a gas mixture of 80% distilled ozone and 20% oxygen. The substrate temperature was maintained at 675 °C during the growth at a chamber pressure of  $5 \times 10^{-6}$  Torr.

**Cross-Section Sample Preparation and High-Angle Annular Dark Field Scanning Transmission Electron Microscopy (HAADF-STEM).** The cross-section samples were prepared using an FEI Helios 660 focused ion beam (FIB) with a gallium (Ga) ion beam source. The cross-section samples were then characterized using an FEI Titan Themis G3 scanning transmission electron microscope (STEM) equipped with double correctors and a monochromator. High-angle annular dark-field scanning transmission electron microscopy (HAADF-STEM) imaging was performed at 300 kV accelerating voltage with a convergence angle of 25 mrad.

**Ion-Milling.** The surface of the film was etched using argon-ion milling (Nanoquest; Intlvac). Once the base pressure dropped below  $5 + 10^{-6}$  Torr, the chamber was filled with argon, maintaining a dynamic partial pressure of  $2.25 + 10^{-4}$  Torr. Etching was performed using a beam voltage of 100 V (~0.7 nm/min), a beam current of 3 mA, and an accelerating voltage of 60 V, while the stage rotated at a speed of 15 rpm and the stage temperature was set to 20 °C.

**NV Magnetometry.** NV images were obtained using a commercially available Qnami Quantum Microscope-ProteusQ™. Parabolic tapered Quantilever™ MX+ diamond tips were chosen for their superior signal-to-noise ratio and photon collection efficiency, making them well-suited for detecting the very small stray fields present in BiFeO<sub>3</sub>. Here, a nitrogen defect along with the nearest neighboring vacancy in negative charge state (NV<sup>-</sup>) is utilized as a single atom quantum sensor by making use of its spin triplet state ( $m_s=0, \mp 1$ ). In our setup, an external magnet is used to break the degeneracy of the  $m_s=\mp 1$  states and a microwave (MW) source frequency is swept to obtain electron spin resonance (ESR) (between  $m_s=0$  to  $m_s=\mp 1$  states) which is then detected optically by measuring photoluminescence (PL) intensity. When the NV diamond tip is scanned through the sample surface, the local stray magnetic field (*B*) projected along the NV<sup>-</sup> axis moves the ESR spectra which is used to track the local magnetic contrast. Here, we have performed imaging in two modes, namely dual iso-*B* and full-*B* (35). In the former, PL is measured at two MW frequencies near the FWHM of the ESR spectra and its difference (PL( $\nu_2$ )-PL( $\nu_1$ )) is used to generate the real space magnetic contrast. In the latter, full ESR spectra is fitted at each point and strength of local magnetic field is estimated quantitatively. To calibrate the orientation of NV<sup>-</sup> center, a known ferromagnetic sample Ta(2 nm)/MgO/CoFeB(0.9 nm)/Ta(5 nm) with perpendicular magnetic anisotropy was used. For more details, we refer to *SI Appendix, section S1*.

**PFM Measurement.** PFM imaging was performed using a Jupiter XR Atomic Force Microscope from Oxford Instruments (Asylum Research). All images were acquired in Dual AC Resonance Tracking (DART) mode, which significantly reduces crosstalk caused by shifts in resonant frequency. This is achieved by tracking the contact resonance frequency and, through a feedback loop, adjusting the drive frequency of the cantilever to maintain resonance. Electric field switching experiments were performed by grounding the bottom SrRuO<sub>3</sub> electrode with silver paint (Ted Pella), while a voltage was applied to the top of BiFeO<sub>3</sub> film using a Pt/Ir-coated conductive tip from Oxford Instruments.

**PE Loop Measurements on Metal-Ferroelectric-Metal Capacitor.** Macroscopic polarization versus electric field measurements were conducted on metal-ferroelectric-metal (M-FE-M) capacitors using a Precision Multiferroic Ferroelectric Tester from Radiant Technologies Inc. The SrRuO<sub>3</sub> layer was used as the bottom electrode, while a platinum layer (~10 nm thick deposited by sputtering at 300 K), patterned into a disc shape, served as the top electrode. For NV measurements on region switched under electrode, a gold (Au) top electrode was used as it could be easily dissolved with an appropriate chemical solution. In the current work, a solution prepared by mixing KI and I<sub>2</sub> in H<sub>2</sub>O was used as solvent.

**Theory.** The dependence of the spin cycloid energy on the propagation vector (Fig. 1A) was computed using the classical spin Hamiltonian of ref. 39. The Hamiltonian

$$H = - \sum_{ij} J_{ij} \mathbf{S}_i \cdot \mathbf{S}_j - \sum_{ij} \mathbf{D}_{ij} \cdot (\mathbf{S}_i \times \mathbf{S}_j) - K \sum_i (S_i^u)^2 \quad [1]$$

includes the symmetric spin exchange interaction up to seventh-nearest neighbors ( $J_{ij}$ ), the Dzyaloshinskii-Moriya (DM) interaction up to third-nearest neighbors ( $D_{ij}$ ) and the easy plane anisotropy ( $K$ ) term. The values of the interaction constants are fitted to density functional theory calculations for the monodomain *R*3c phase of BiFeO<sub>3</sub> (39). The DM vectors are given by the converse spin-current model  $\mathbf{D}_{ij} = (\mathbf{u} \times \mathbf{e}_{ij})$ , where  $\mathbf{u}$  denotes the unit vector oriented along the pseudocubic  $[\bar{1}\bar{1}\bar{1}]$  axis and  $\mathbf{e}_{ij}$  are unit vectors connecting spins at sites  $i$  and  $j$ .  $S_i^u$  denotes the  $[\bar{1}\bar{1}\bar{1}]$  projection of the spin.

The energy is computed assuming the following spin cycloid ansatz

$$\mathbf{S}_i = \cos((\mathbf{Q}_R + \mathbf{q}) \cdot \mathbf{r}_i) \mathbf{u} + \sin((\mathbf{Q}_R + \mathbf{q}) \cdot \mathbf{r}_i) \mathbf{e}_q, \quad [2]$$

where  $\mathbf{Q}_R$  denotes the  $R$  point coordinates of the pseudocubic BZ while  $\mathbf{e}_q$  stands for the unit vector in the direction of the cycloid propagation vector  $\mathbf{q}$ . An analytical energy expression  $E(\mathbf{q})$  is obtained by substituting Eq. 2 into Eq. 1. Fig. 1A shows the plot of the energy difference  $\Delta E = E(\mathbf{q}) - E(\mathbf{0})$  between the energies of the AFM spin cycloid ( $\mathbf{q} \neq \mathbf{0}$ ) and G-AFM states ( $\mathbf{q} = \mathbf{0}$ ) for propagation vector  $\mathbf{q}$  lying within the (111) plane.

**Data, Materials, and Software Availability.** All study data are included in the article and/or *SI Appendix*.

**ACKNOWLEDGMENTS.** S.K.O., X.L., L.W.M., Y.H., and R.R. acknowledge support by the National Science Foundation Future Semiconducting Electronics (FUSE) program under Grant DMR-2329111. S.H. was supported by the US Department of Energy, Office of Science, Office of Basic Energy Sciences,

Materials Sciences and Engineering Division under Contract No. DE-AC02-05-CH11231. S.H., L.W.M., and R.R. additionally acknowledge that this research was sponsored by the Army Research Laboratory and was accomplished under Cooperative Agreement Number W911NF-24-2-0100. M.R., D.G.S., S.P., Y.N., and L.B. acknowledge the support of the Army Research Office under the Emergent Topological and Hierarchical Structures-Multidisciplinary University Research Initiative (ETHOS MURI) via cooperative agreement W911NF-21-2-0162. D.K. acknowledges the support from the National Science Foundation under Grant DMR-2102895. X.L. acknowledges additional support from the Rice Advanced Materials Institute (RAMI) at Rice University as a RAMI Postdoctoral Fellow. X.L. and Y.H. additionally acknowledge the support from the National Science Foundation under Grant CMMI-2239545 and the Welch Foundation under Grant C-2065). S.P., Y.N., and L.B. also thank the Vannevar Bush Faculty Fellowship Grant No. N00014-20-1-2834 from the Department of Defense, the MonArk NSF Quantum Foundry supported by the NSF Quantum Materials Science, Engineering and Information (Q-AMASE-i) Program under NSF Award No. DMR-1906383, and an Impact Grant from ARA. The theoretical calculations were performed at the Arkansas High Performance Computing Center. C.-B.E. acknowledges support for this research through a Vannevar Bush Faculty Fellowship (ONRN00014-20-1-2844), the Gordon and the Betty Moore Foundation's Emergent Phenomena in Quantum Systems Initiative, Grant GBMF9065. Ferroelectric and structural measurements at the University of Wisconsin-Madison was supported by the US Department of Energy, Office of Science, Office of Basic Energy Sciences, under award number DE-FG02-06ER46327. The views and conclusions contained in this document are those of the authors and should not be interpreted as representing the official policies, either expressed or implied, of the Army Research Laboratory or the US Government. The US Government is authorized to reproduce and distribute reprints for Government purposes notwithstanding any copyright notation herein.

Author affiliations: <sup>a</sup>Rice Advanced Materials Institute, Rice University, Houston, TX 77005; <sup>b</sup>Department of Materials Science and NanoEngineering, Rice University, Houston, TX 77005; <sup>c</sup>Department of Materials Science and Engineering, University of Wisconsin-Madison, Madison, WI 53706; <sup>d</sup>Department of Physics and Institute for Nanoscience and Engineering, Smart Ferroic Materials Center, University of Arkansas, Fayetteville, AR 72701; <sup>e</sup>Department of Materials Science and Engineering, University of California, Berkeley, CA 94720; <sup>f</sup>Department of Materials Science and Engineering, Cornell University, Ithaca, NY 14853; <sup>g</sup>Kavli Institute at Cornell for Nanoscale Science, Cornell University, Ithaca, NY 14853; <sup>h</sup>Leibniz-Institut für Kristallzüchtung, Berlin 12489, Germany; <sup>i</sup>Department of Physics, Northeastern University, Boston, MA 02115; <sup>j</sup>Department of Physics, School of Engineering, Brown University, Providence, RI 02912; <sup>k</sup>Departments of Chemistry, Rice University, Houston, TX 77005; <sup>l</sup>Departments of Physics and Astronomy, Rice University, Houston, TX 77005; <sup>m</sup>Department of Materials Science and Engineering, Tel Aviv University, Ramat Aviv, Tel Aviv 6997801, Israel; <sup>n</sup>Materials Sciences Division, Lawrence Berkeley National Laboratory, Berkeley, CA 94720; and <sup>o</sup>Department of Physics, University of California, Berkeley, CA 94720

1. A. M. Turing, The chemical basis of morphogenesis. *Bull. Math. Biol.* **52**, 153-197 (1990).
2. M. C. Cross, P. C. Hohenberg, Pattern formation outside of equilibrium. *Rev. Mod. Phys.* **65**, 851-1112 (1993).
3. D. Walgraef, *Spatio-Temporal Pattern Formation: with Examples from Physics, Chemistry, and Materials Science* (Springer Science & Business Media, 2012).
4. M. Cross, H. Greenside, *Pattern Formation and Dynamics in Nonequilibrium Systems* (Cambridge University Press, 2009).
5. A. J. Koch, H. Meinhardt, Biological pattern formation: From basic mechanisms to complex structures. *Rev. Mod. Phys.* **66**, 1481-1507 (1994).
6. Y. Fuseya, H. Katsuno, K. Behnia, A. Kapitulnik, Nanoscale turing patterns in a bismuth monolayer. *Nat. Phys.* **17**, 1031-1036 (2021).
7. W. H. Zurek, Cosmological experiments in condensed matter systems. *Phys. Rep.* **276**, 177-221 (1996).
8. T. Kibble, Phase-transition dynamics in the lab and the universe. *Phys. Today* **60**, 47-52 (2007).
9. N. D. Mermin, The topological theory of defects in ordered media. *Rev. Mod. Phys.* **51**, 591-648 (1979).
10. M. J. Lyons, L. G. Harrison, Stripe selection: An intrinsic property of some pattern-forming models with nonlinear dynamics. *Dev. Dyn.* **195**, 201-215 (1992).
11. J. M. Kosterlitz, D. J. Thouless, Long range order and metastability in two dimensional solids and superfluids. (Application of dislocation theory). *J. Phys. C Solid State Phys.* **5**, L124 (1972).
12. J. M. Kosterlitz, D. J. Thouless, Ordering, metastability and phase transitions in two-dimensional systems. *J. Phys. C Solid State Phys.* **6**, 1181 (1973).
13. B. I. Halperin, D. R. Nelson, Theory of two-dimensional melting. *Phys. Rev. Lett.* **41**, 121-124 (1978).
14. A. P. Young, Melting and the vector coulomb gas in two dimensions. *Phys. Rev. B* **19**, 1855-1866 (1979).
15. M. Seul, R. Wolfe, Evolution of disorder in magnetic stripe domains. I. Transverse instabilities and disclination unbinding in lamellar patterns. *Phys. Rev. A* **46**, 7519-7533 (1992).
16. P. Schoenher et al., Topological domain walls in helimagnets. *Nat. Phys.* **14**, 465-468 (2018).
17. A. Fert, N. Reyren, V. Cros, Magnetic skyrmions: Advances in physics and potential applications. *Nat. Rev. Mater.* **2**, 17031 (2017).
18. O. J. Amin et al., Antiferromagnetic half-skyrmions electrically generated and controlled at room temperature. *Nat. Nanotechnol.* **18**, 849-853 (2023).
19. N. Nagaosa, Y. Tokura, Topological properties and dynamics of magnetic skyrmions. *Nat. Nanotechnol.* **8**, 899-911 (2013).
20. S. Das et al., Observation of room-temperature polar skyrmions. *Nature* **568**, 368-372 (2019).
21. V. Govinden et al., Ferroelectric solitons crafted in epitaxial bismuth ferrite superlattices. *Nat. Commun.* **14**, 4178 (2023).
22. A. Nych, J.-I. Fukuda, U. Ognysta, S. Žumer, I. Mušević, Spontaneous formation and dynamics of half-skyrmions in a chiral liquid-crystal film. *Nat. Phys.* **13**, 1215-1220 (2017).
23. P. J. Ackerman, T. Boyle, I. I. Smalyukh, Squirming motion of baby skyrmions in nematic fluids. *Nat. Commun.* **8**, 673 (2017).
24. A. Finco et al., Imaging topological defects in a noncollinear antiferromagnet. *Phys. Rev. Lett.* **128**, 187201 (2022).
25. A. Chaudron et al., Electric-field-induced multiferroic topological solitons. *Nat. Mater.* **23**, 905-911 (2024).
26. A. Fert, R. Ramesh, V. Garcia, F. Casanova, M. Bibes, Electrical control of magnetism by electric field and current-induced torques. *Rev. Mod. Phys.* **96**, 015005 (2024).
27. M. Bibes, A. Barthélémy, Towards a magnetoelectric memory. *Nat. Mater.* **7**, 425-426 (2008).
28. J. T. Heron et al., Deterministic switching of ferromagnetism at room temperature using an electric field. *Nature* **516**, 370-373 (2014).

29. S. Manipatruni *et al.*, Scalable energy-efficient magnetoelectric spin-orbit logic. *Nature* **565**, 35–42 (2019).
30. E. Parsonnet *et al.*, Nonvolatile electric field control of thermal magnons in the absence of an applied magnetic field. *Phys. Rev. Lett.* **129**, 087601 (2022).
31. X. Huang *et al.*, Manipulating chiral spin transport with ferroelectric polarization. *Nat. Mater.* **23**, 898–904 (2024).
32. S. Husain *et al.*, Non-volatile magnon transport in a single domain multiferroic. *Nat. Commun.* **15**, 5966 (2024).
33. J. M. Moreau, C. Michel, R. Gerson, W. J. James, Ferroelectric BiFeO<sub>3</sub> X-ray and neutron diffraction study. *J. Phys. Chem. Solids* **32**, 1315–1320 (1971).
34. I. Sosnowska, T. P. Neumaier, E. Steichele, Spiral magnetic ordering in bismuth ferrite. *J. Phys. C Solid State Phys.* **15**, 4835 (1982).
35. I. Gross *et al.*, Real-space imaging of non-collinear antiferromagnetic order with a single-spin magnetometer. *Nature* **549**, 252–256 (2017).
36. P. Meisenheimer *et al.*, Switching the spin cycloid in BiFeO<sub>3</sub> with an electric field. *Nat. Commun.* **15**, 2903 (2024).
37. S. R. Burns, O. Paull, J. Juraszek, V. Nagarajan, D. Sando, The experimentalist's guide to the cycloid, or noncollinear antiferromagnetism in epitaxial BiFeO<sub>3</sub>. *Adv. Mater.* **32**, 2003711 (2020).
38. R. D. Johnson *et al.*, X-ray imaging and multiferroic coupling of cycloidal magnetic domains in ferroelectric monodomain BiFeO<sub>3</sub>. *Phys. Rev. Lett.* **110**, 217206 (2013).
39. S. Meyer, B. Xu, M. J. Verstraete, L. Bellaiche, B. Dupé, Spin-current driven Dzyaloshinskii-Moriya interaction in multiferroic BiFeO<sub>3</sub> from first principles. *Phys. Rev. B* **108**, 024403 (2023).
40. P. Dufour *et al.*, Onset of multiferroicity in prototypical single-spin cycloid BiFeO<sub>3</sub> thin films. *Nano Lett.* **23**, 9073–9079 (2023).
41. S. Echeverría-Alar, M. G. Clerc, Labyrinthine patterns transitions. *Phys. Rev. Res.* **2**, 042036 (2020).
42. N. Waterfield Price *et al.*, Coherent magnetoelastic domains in multiferroic BiFeO<sub>3</sub> films. *Phys. Rev. Lett.* **117**, 177601 (2016).
43. J. R. Maze *et al.*, Nanoscale magnetic sensing with an individual electronic spin in diamond. *Nature* **455**, 644–647 (2008).
44. L. Rondin *et al.*, Magnetometry with nitrogen-vacancy defects in diamond. *Rep. Prog. Phys.* **77**, 056503 (2014).
45. Y. Nahas *et al.*, Topology and control of self-assembled domain patterns in low-dimensional ferroelectrics. *Nat. Commun.* **11**, 5779 (2020).
46. J. Junquera *et al.*, Topological phases in polar oxide nanostructures. *Rev. Mod. Phys.* **95**, 025001 (2023).
47. M. Le Berre, E. Ressayre, A. Tallet, Y. Pomeau, L. Di Menza, Example of a chaotic crystal: The labyrinth. *Phys. Rev. E* **66**, 026203 (2002).
48. Z. Li *et al.*, Multiferroic skyrmions in BiFeO<sub>3</sub>. *Phys. Rev. Res.* **5**, 043109 (2023).
49. H. Zhong *et al.*, Quantitative imaging of exotic antiferromagnetic spin cycloids in BiFeO<sub>3</sub> thin films. *Phys. Rev. Appl.* **17**, 044051 (2022).
50. R. Liu, S. Liaw, P. Maini, Oscillatory Turing patterns in a simple reaction-diffusion system. *J. Korean Phys. Soc.* **50**, 234–238 (2007).
51. T. Mullin, T. J. Price, An experimental observation of chaos arising from the interaction of steady and time-dependent flows. *Nature* **340**, 294–296 (1989).
52. K. I. Agladze, V. I. Krinsky, A. M. Pertsov, Chaos in the non-stirred Belousov-Zhabotinsky reaction is induced by interaction of waves and stationary dissipative structures. *Nature* **308**, 834–835 (1984).
53. P. M. Chaikin, T. C. Lubensky, *Principles of Condensed Matter Physics* (Cambridge University Press, Cambridge, 1995).
54. T. Nagase *et al.*, Observation of domain wall bimerons in chiral magnets. *Nat. Commun.* **12**, 3490 (2021).
55. M. J. Gim, D. A. Beller, D. K. Yoon, Morphogenesis of liquid crystal topological defects during the nematic-smectic a phase transition. *Nat. Commun.* **8**, 15453 (2017).
56. L. Giomi, Ž. Kos, M. Ravnik, A. Sengupta, Cross-talk between topological defects in different fields revealed by nematic microfluidics. *Proc. Natl. Acad. Sci. U.S.A.* **114**, E5771–E5777 (2017).
57. M. Merle, L. Messio, J. Mozziconacci, Turing-like patterns in an asymmetric dynamic Ising model. *Phys. Rev. E* **100**, 042111 (2019).
58. S. Zakany, S. Smirnov, M. C. Milinkovitch, Lizard skin patterns and the Ising model. *Phys. Rev. Lett.* **128**, 048102 (2022).
59. Y. Dovzhenko *et al.*, Magnetostatic twists in room-temperature skyrmions explored by nitrogen-vacancy center spin texture reconstruction. *Nat. Commun.* **9**, 2712 (2018).
60. B. C. Jeon *et al.*, Flexoelectric effect in the reversal of self-polarization and associated changes in the electronic functional properties of BiFeO<sub>3</sub> thin films. *Adv. Mater.* **25**, 5643–5649 (2013).
61. T. Yang *et al.*, The evidence of giant surface flexoelectric field in (111) oriented BiFeO<sub>3</sub> thin film. *ACS Appl. Mater. Interfaces* **9**, 5600–5606 (2017).
62. F. Bernardini, M. Fiebig, A. Cano, Ruddlesden-popper and perovskite phases as a material platform for altermagnetism. *arXiv [Preprint]* (2024). <http://arxiv.org/abs/2401.12910> (Accessed 2 September 2024).
63. L. Šmejkal, Altermagnetic multiferroics and altermagnetoelectric effect. *arXiv [Preprint]* (2024). <https://doi.org/10.48550/arXiv.2411.19928> (Accessed 6 April 2025).
64. W. Saenrang *et al.*, Deterministic and robust room-temperature exchange coupling in monodomain multiferroic BiFeO<sub>3</sub> heterostructures. *Nat. Commun.* **8**, 1583 (2017).
65. S. H. Baek *et al.*, Ferroelastic switching for nanoscale non-volatile magnetoelectric devices. *Nat. Mater.* **9**, 309–314 (2010).

# Supplementary Information

## Morphogenesis of spin cycloids in a noncollinear antiferromagnet

**Shashank Kumar Ojha**<sup>1,11,\*</sup>, **Pratap Pal**<sup>2</sup>, **Sergei Prokhorenko**<sup>3</sup>, **Sajid Husain**<sup>4,\*</sup>, **Maya Ramesh**<sup>5</sup>, **Xinyan Li**<sup>1,11</sup>, **Deokyoung Kang**<sup>1,6</sup>, **Peter Meisenheimer**<sup>6</sup>, **Darrell G. Schlom**<sup>5,7,8</sup>, **Paul Stevenson**<sup>9,\*</sup>, **Lucas Caretta**<sup>10</sup>, **Yusra Nahas**<sup>3</sup>, **Yimo Han**<sup>1,11</sup>, **Lane W. Martin**<sup>1,4,11,12</sup>, **Laurent Bellaiche**<sup>3,13</sup>, **Chang-Beom Eom**<sup>2</sup>, **Ramamoorthy Ramesh**<sup>1,4,6,11,12,14,\*</sup>

<sup>1</sup>Rice Advanced Materials Institute, Rice University, Houston, TX, 77005, USA

<sup>2</sup>Department of Materials Science and Engineering, University of Wisconsin-Madison, Madison, WI 53706, USA

<sup>3</sup>Smart Ferroic Materials Center, Physics Department and Institute for Nanoscience and Engineering, University of Arkansas, Fayetteville, Arkansas, USA

<sup>4</sup>Materials Sciences Division, Lawrence Berkeley National Laboratory, Berkeley, CA, 94720, USA

<sup>5</sup>Department of Materials Science and Engineering, Cornell University, Ithaca, NY, 14853, USA

<sup>6</sup>Department of Materials Science and Engineering, University of California, Berkeley, CA, 94720, USA

<sup>7</sup>Kavli Institute at Cornell for Nanoscale Science, Cornell University, Ithaca, NY, 14853, USA

<sup>8</sup>Leibniz-Institut für Kristallzüchtung, Max-Born-Str. 2, 12489, Berlin, Germany

<sup>9</sup>Department of Physics, Northeastern University, Boston, MA 02115, USA

<sup>10</sup>School of Engineering, Brown University, Providence, RI, USA

<sup>11</sup>Department of Materials Science and NanoEngineering, Rice University, Houston, TX, 77005, USA

<sup>12</sup>Departments of Chemistry and Physics and Astronomy, Rice University, Houston, TX, 77005, USA

<sup>13</sup>Department of Materials Science and Engineering, Tel Aviv University, Ramat Aviv, Tel Aviv 6997801, Israel

<sup>14</sup>Department of Physics, University of California, Berkeley, CA, 94720, USA

\*so37@rice.edu

\*p.stevenson@northeastern.edu

\*rramesh@berkeley.edu

\*shusain@berkeley.edu

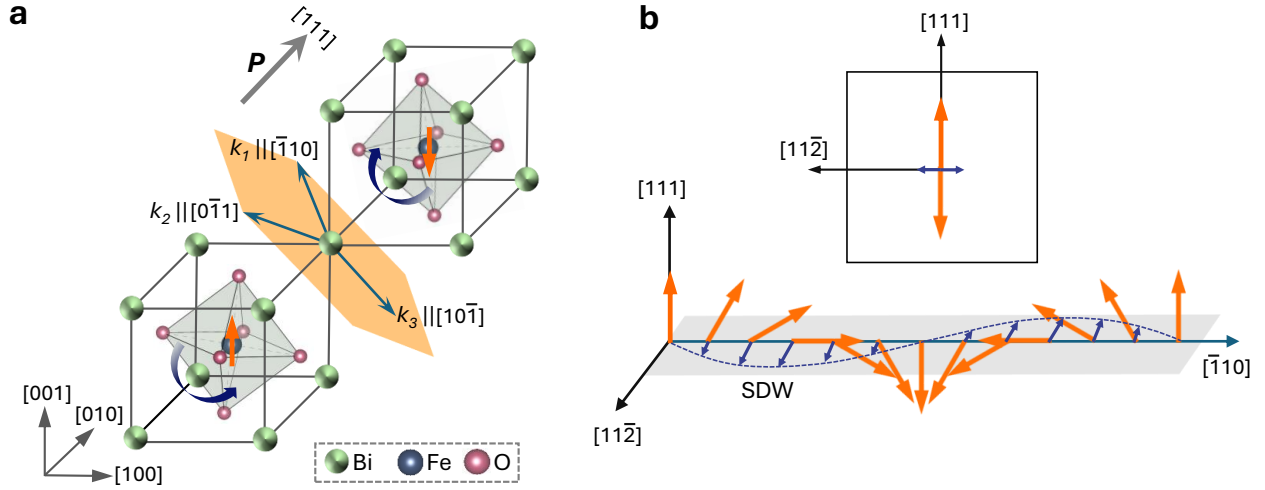


**Fig. S 1. BiFeO<sub>3</sub> unit cell, structure of spin cycloid and spin density wave (SDW)**  
 (a) Two corner shared pseudocubic unit cells which constitute the rhombohedral lattice of BiFeO<sub>3</sub>. Ferroelectric Polarization ( $\mathbf{P}$ ) is shown along the [111] direction. All crystallographic directions are in pseudocubic notations. In principle,  $\mathbf{P}$  could point along any of the body diagonals.  $k_1$ ,  $k_2$  and  $k_3$  denote the three equivalent directions for the propagation of antiferromagnetic spin cycloids in the bulk of BiFeO<sub>3</sub>. For each  $k$ ,  $-k$  is the degenerate pair. Orange arrows depict magnetic moment on Fe atoms. Antiferrodistortive rotation of oxygen octahedra is shown with blue curved arrows.  
 (b) Structure of spin cycloid along with spin density wave. Here the continuous cycloidal rotation of iron moments (orange arrows) in the  $\mathbf{P}$ - $\mathbf{k}$  plane leads to the formation of spin cycloids.

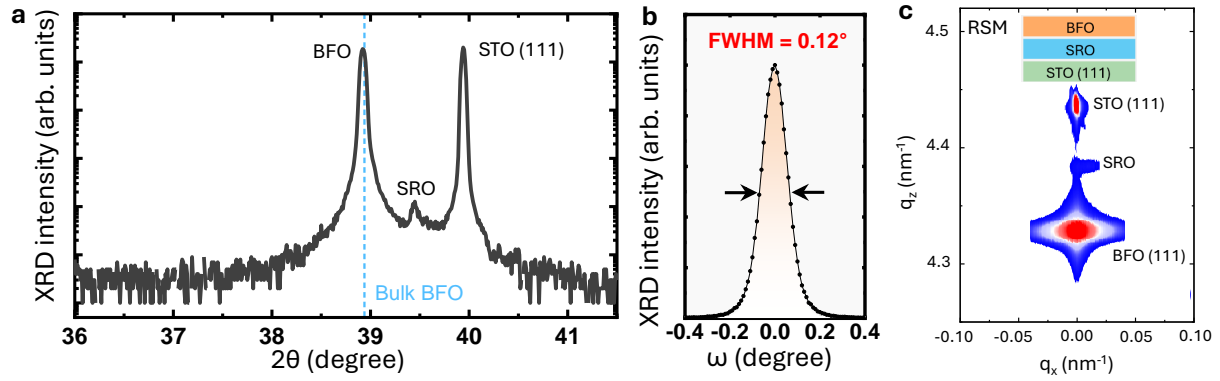


**Fig. S 2.** (a) X-ray diffraction pattern of a 1000 nm  $\text{BiFeO}_3/\text{SrRuO}_3/\text{SrTiO}_3$  (111) heterostructure around (111) peak of STO. (b) Rocking curve of (111)  $\text{BiFeO}_3$  peak. (c) Reciprocal space map taken around (111) peak.

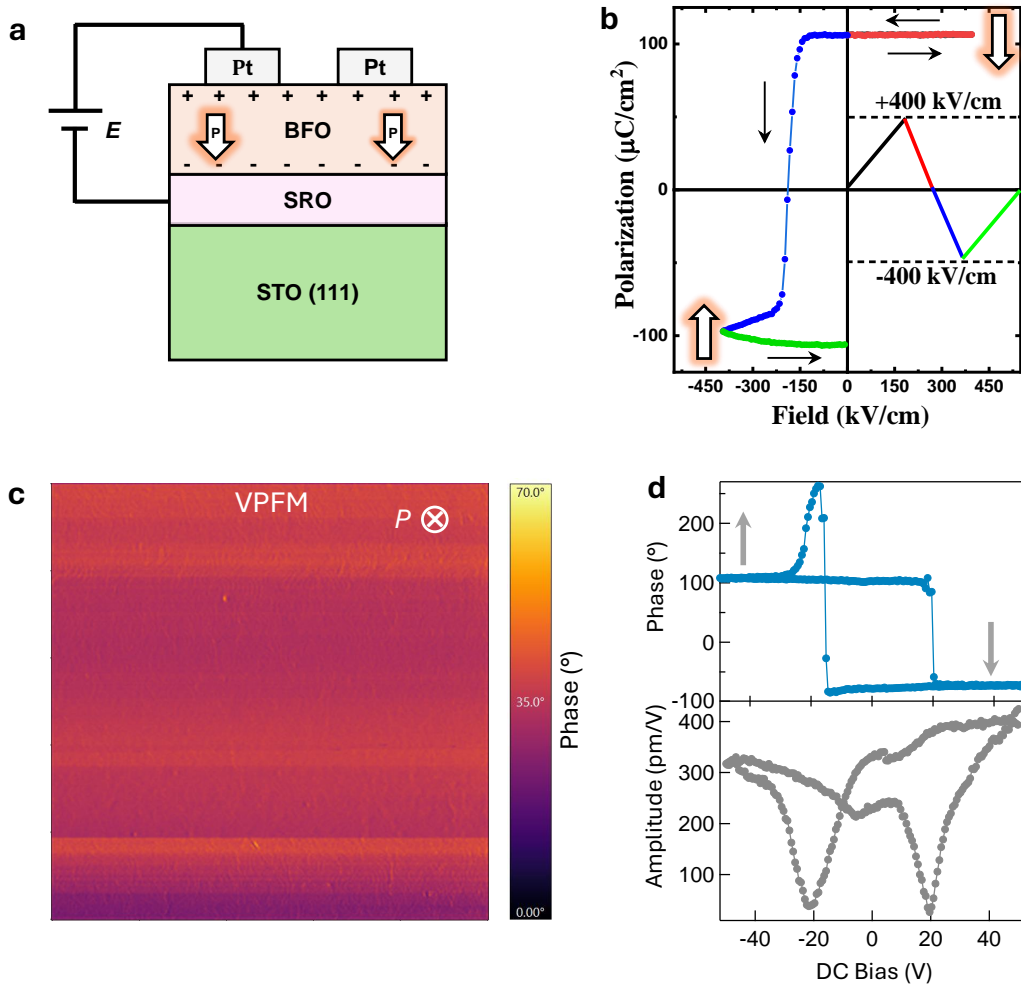


**Fig. S 3.** (a) Metal-ferroelectric-metal structure used for measuring polarization vs electric field hysteresis. Here  $\text{SrRuO}_3$  layer serves as bottom electrode and platinum as top electrode. (b) Polarization vs electric field hysteresis loop measured on a 1000 nm  $\text{BiFeO}_3/\text{SrRuO}_3/\text{SrTiO}_3$  (111) sample. Inset shows the voltage ramping protocol for measuring hysteresis. (c) Piezo force microscopy phases taken in vertical channel. As evident, the variation in phase is very small over large scales demonstrating single ferroelectric domain. The as grown direction of the polarization is into the plane i.e.  $[\bar{1}\bar{1}\bar{1}]$ . This is also evident from the point-contact piezoelectric hysteresis (d) which exhibits a complete  $180^\circ$  phase reversal (from  $-90^\circ$  to  $+90^\circ$ ) upon switching the electric field direction from  $[\bar{1}\bar{1}\bar{1}]$  to  $[111]$ .

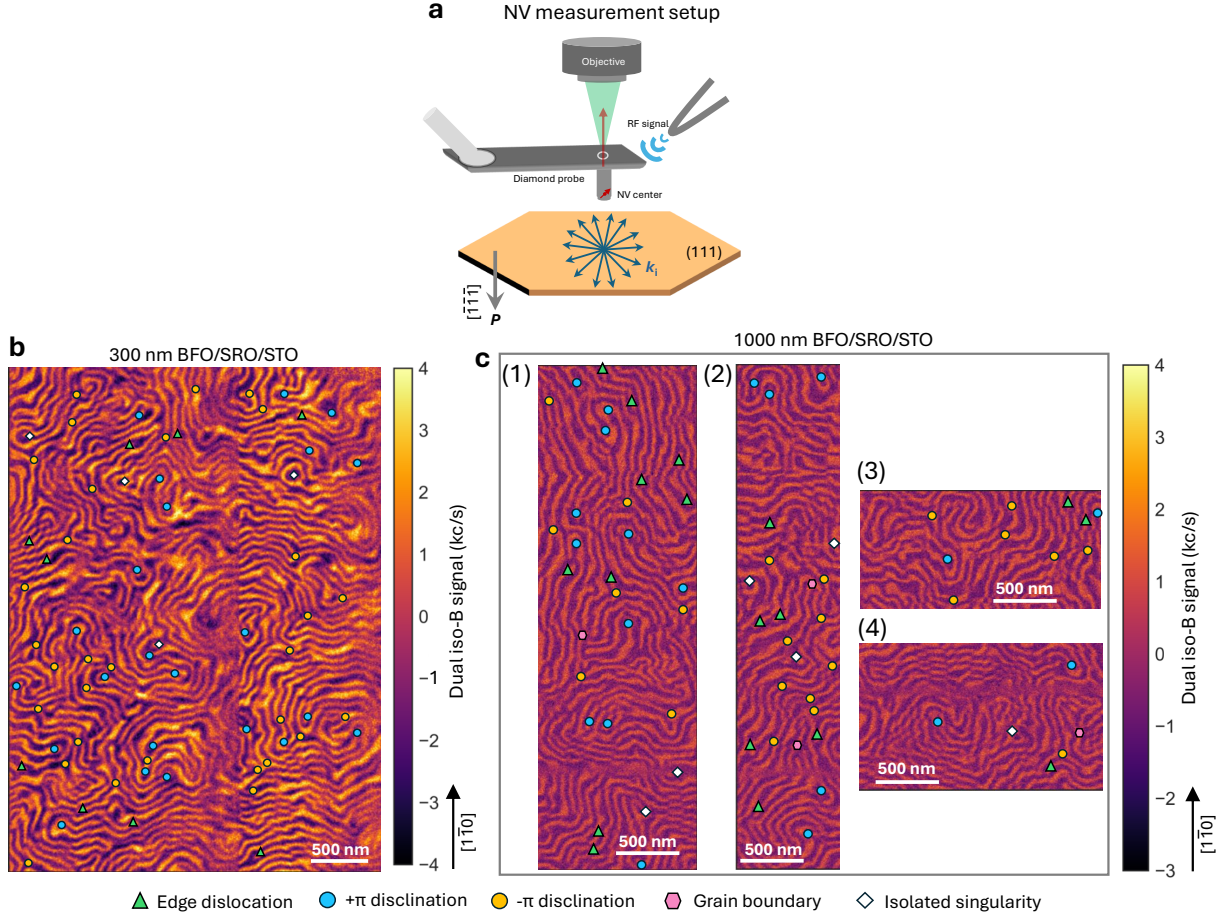


**Fig. S 4.** (a) Schematic of the nitrogen-vacancy diamond-based scanning probe magnetometry used to image spin cycloids on (111) surface of  $\text{BiFeO}_3$  films. A representative (111) surface of  $\text{BiFeO}_3$  being imaged is shown in the bottom panel.  $[\bar{1}\bar{1}\bar{1}]$  is the direction of the spontaneous polarization in the as-grown  $\mathbf{P}$ -state for our system. Light blue arrows on (111) plane represent the equiaxial  $k$ -vector of the spin cycloid within the (111) plane. Additional dual iso- $B$  images taken on 300 nm (panel (b)) and 1000 nm (panel (c)) thick  $\text{BiFeO}_3$  samples. Distribution of different types of topological defects have been marked with different symbols as done in the main text.

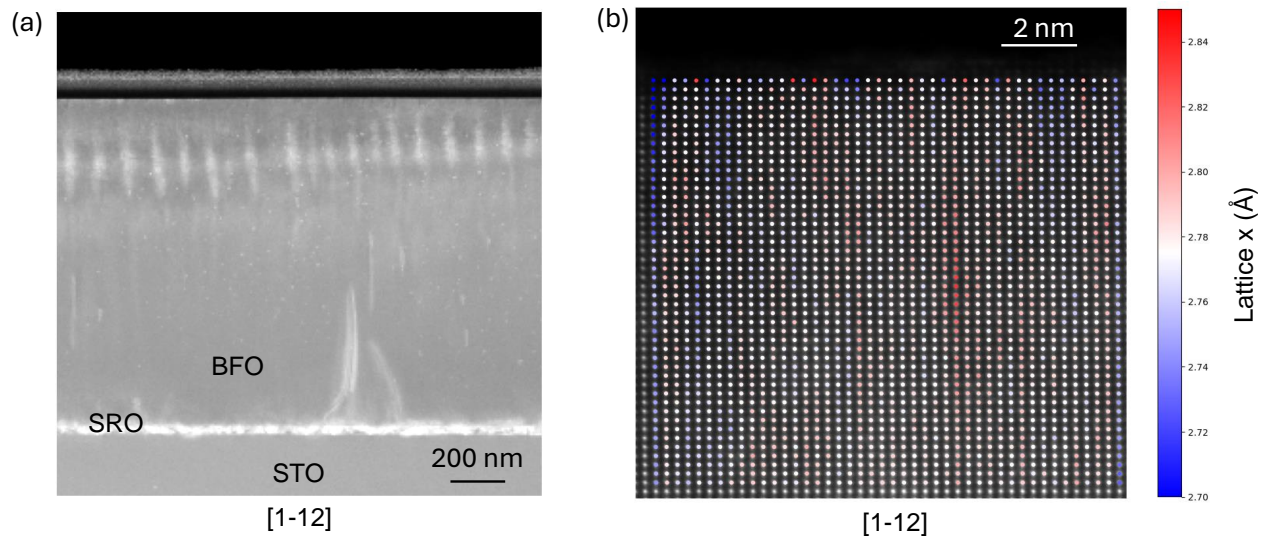


**Fig. S 5.** (a) Atomic-scale lattice mapping of BFO along [1-12] zone axis. (b) Variation of in-plane lattice constant obtained from Cross sectional HAADF-STEM image taken near the surface and also overlaid onto the HAADF-STEM image. Atomic positions were obtained by multiple-ellipse fitting [1] to calculate the lattice length between adjacent Bi atoms.

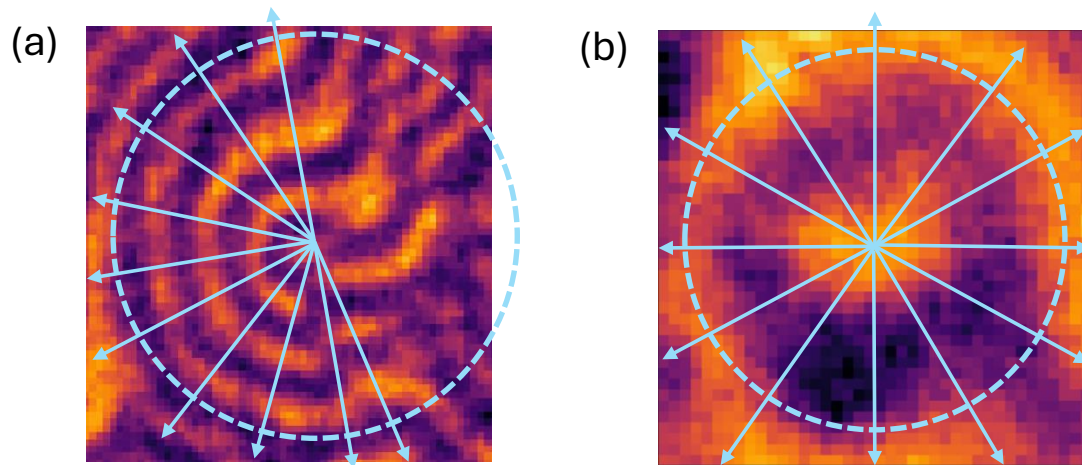


**Fig. S 6.** (a) Section of magnetic texture on (111) surface of BFO. Sky blue color arrows represent the range of propagation vectors observed for cycloid. (b) Similar plot near an isolated spot.

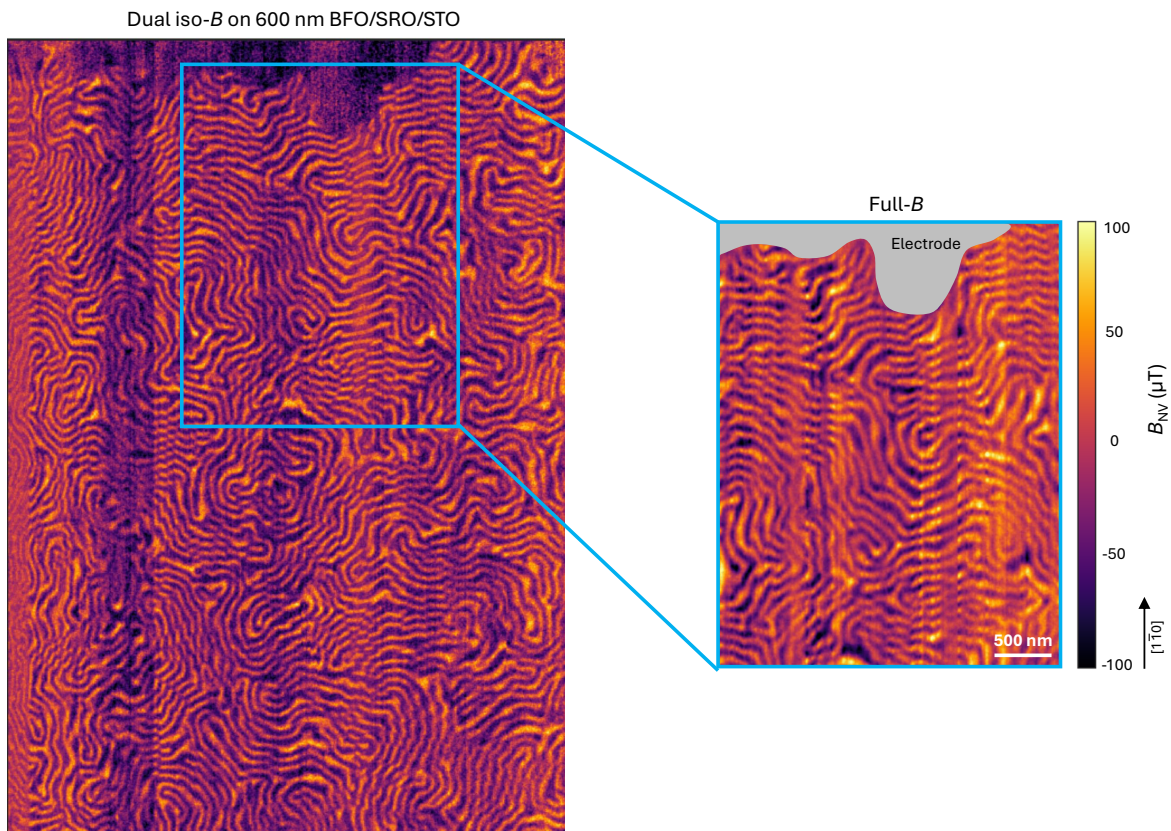


**Fig. S 7.** Additional full- $B$  image taken on 600 nm thick BiFeO<sub>3</sub> film. Top region covered with slate gray color is the region with platinum electrode.

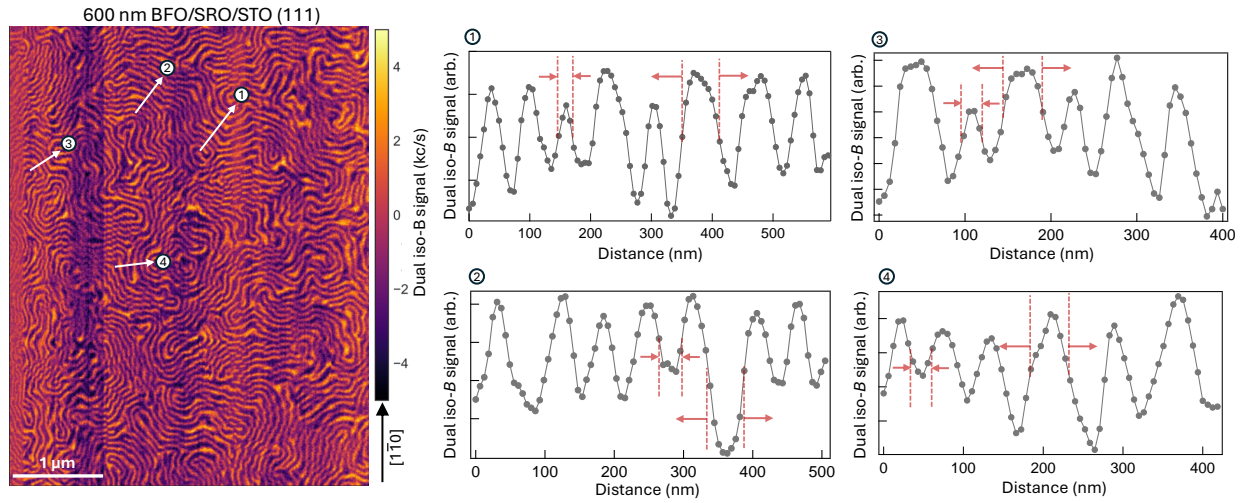


**Fig. S 8.** Line scans taken along four random directions shown with white arrows. Here, we have deliberately chosen only those regions which have coherent local cycloidal order. Panels numbered 1-4 (in right side) show the corresponding evolution of cycloids along line-scans. As evident, there are variations in the periodicity of cycloids demonstrating morphogenesis even at local scales.

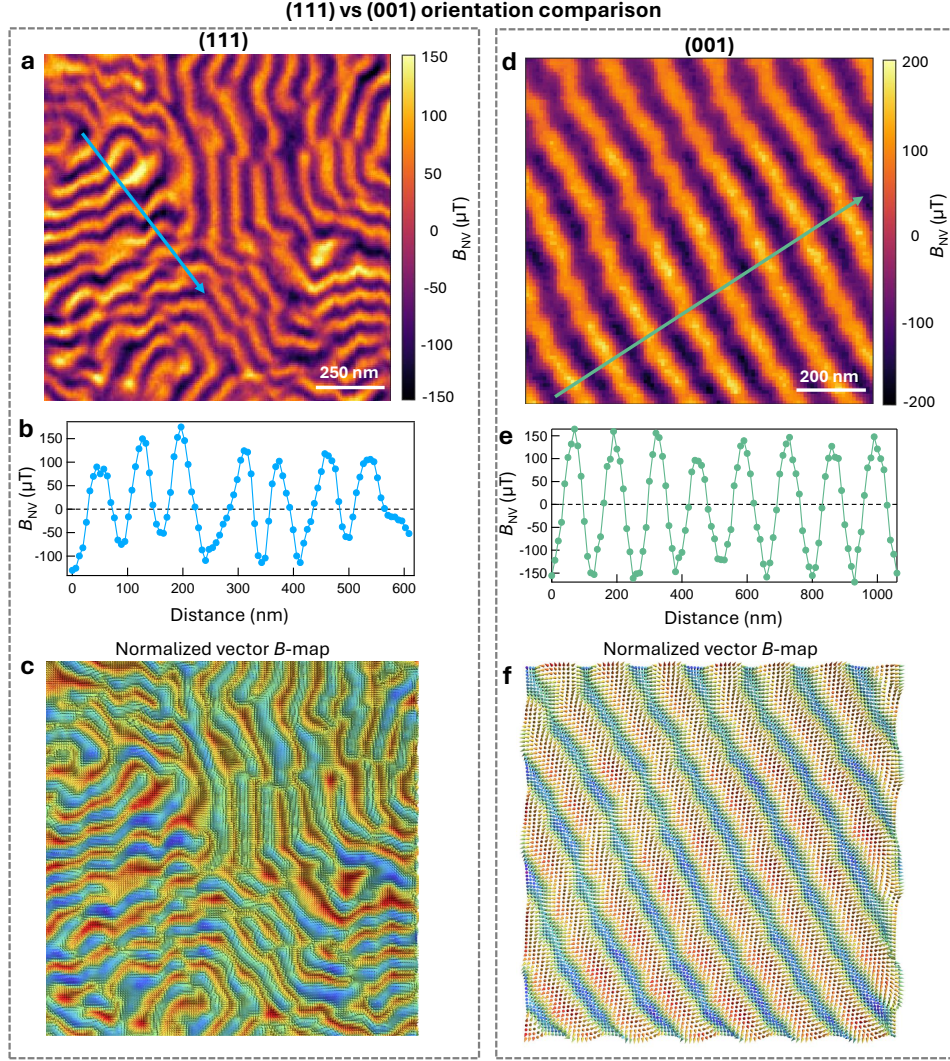


**Fig. S 9. Comparison between (111) and (001) oriented  $\text{BiFeO}_3$  films:** To validate the variation of cycloid periodicity inferred from the analysis of dual iso  $B$  signal (shown in the Supplementary Fig. S8), we have also analyzed the Full- $B$  data (panel (a)). In panel (b) we present the variation in the magnitude of the stray magnetic field taken along a line scan (shown with the sky blue color arrow in the panel (a)) As is evident, there is drastic variation in the cycloid periodicity thereby validating our claim. To gain further insight, we constructed stray  $B$ -field vector maps of spin cycloids, leveraging the linear dependence of  $B$ -field components in Fourier space [2–4]. This allows reconstruction of the full vector map from a single measurement along the axis parallel to the  $\text{NV}^-$  center (Supplementary Information section S1). In the panel (c), we display the normalized vector map of the same region (panel (a)). As is evident, there is variation not only in the width of the cycloids but also in the magnitude of local stray field, which changes from one cycloid to another. To demonstrate that this is a unique feature of the (111) surface, we have also recorded a full- $B$  measurement on a 100 nm thick (001) oriented  $\text{BiFeO}_3$  grown on  $\text{TbScO}_3$  substrate (panel (d)). (e) A line scan taken along a green arrow (shown in the panel (d)) exhibits the homogeneous width of the cycloid. For qualitative comparison, in panel (f) we also show a similar normalized  $B$ -field vector map of the same region shown in panel (d). This film exhibits nearly ordered cycloids, further highlighting the critical role of degeneracy in the cycloid propagation vector in driving the spatial organization of cycloids in (111)-oriented  $\text{BiFeO}_3$ .

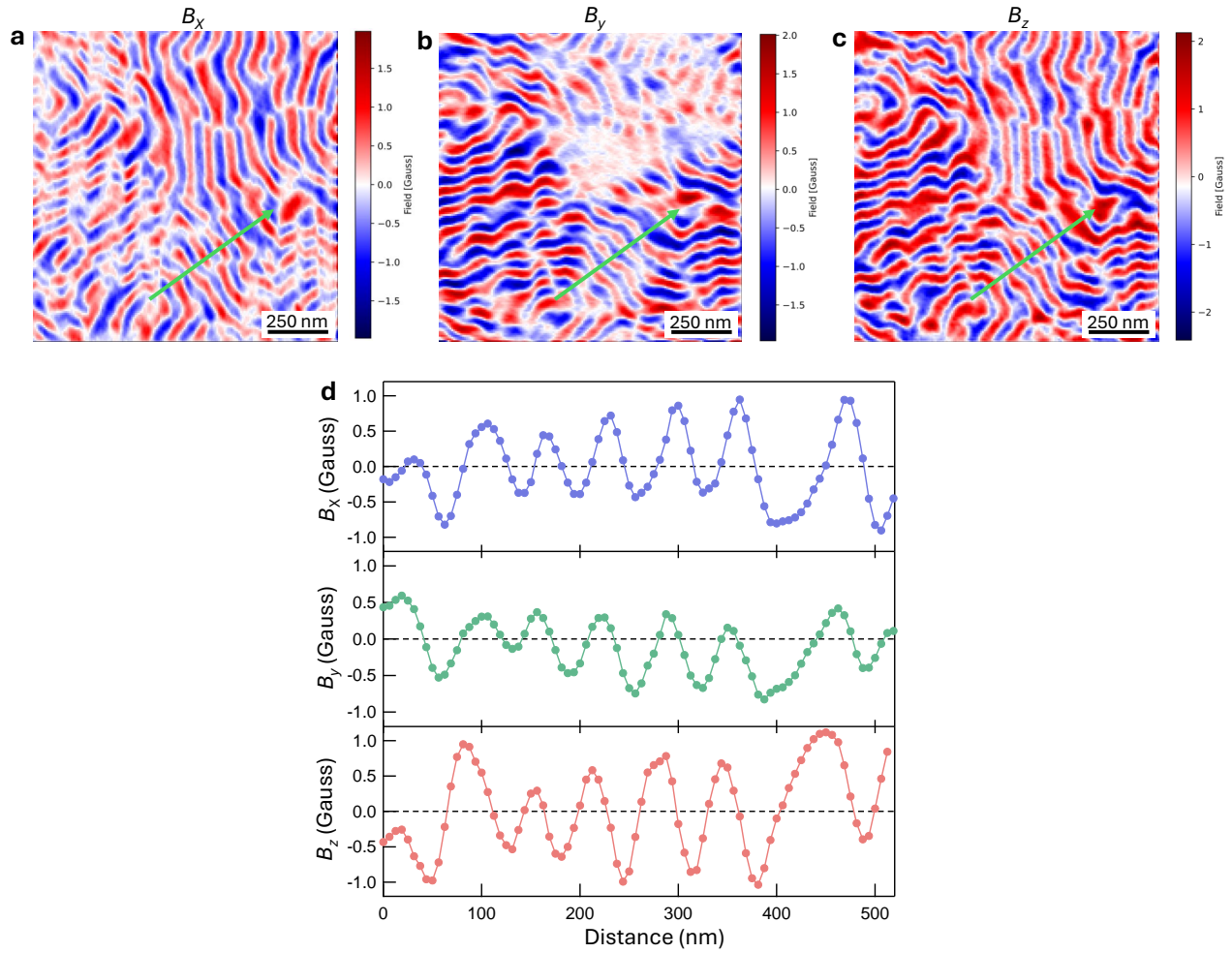


**Fig. S 10. Full- $B$  reconstruction of the region shown in the panel (a) of Supplementary Fig. S9:** (a-c)  $x$ ,  $y$  and  $z$  components of the stray magnetic field reconstructed in the region shown in the panel (a) of Supplementary Fig. S9. Green line shows the direction along which a line scan was taken to show the spatial modulation of the individual  $x$ ,  $y$  and  $z$  components (panel (d)) of the stray magnetic field.

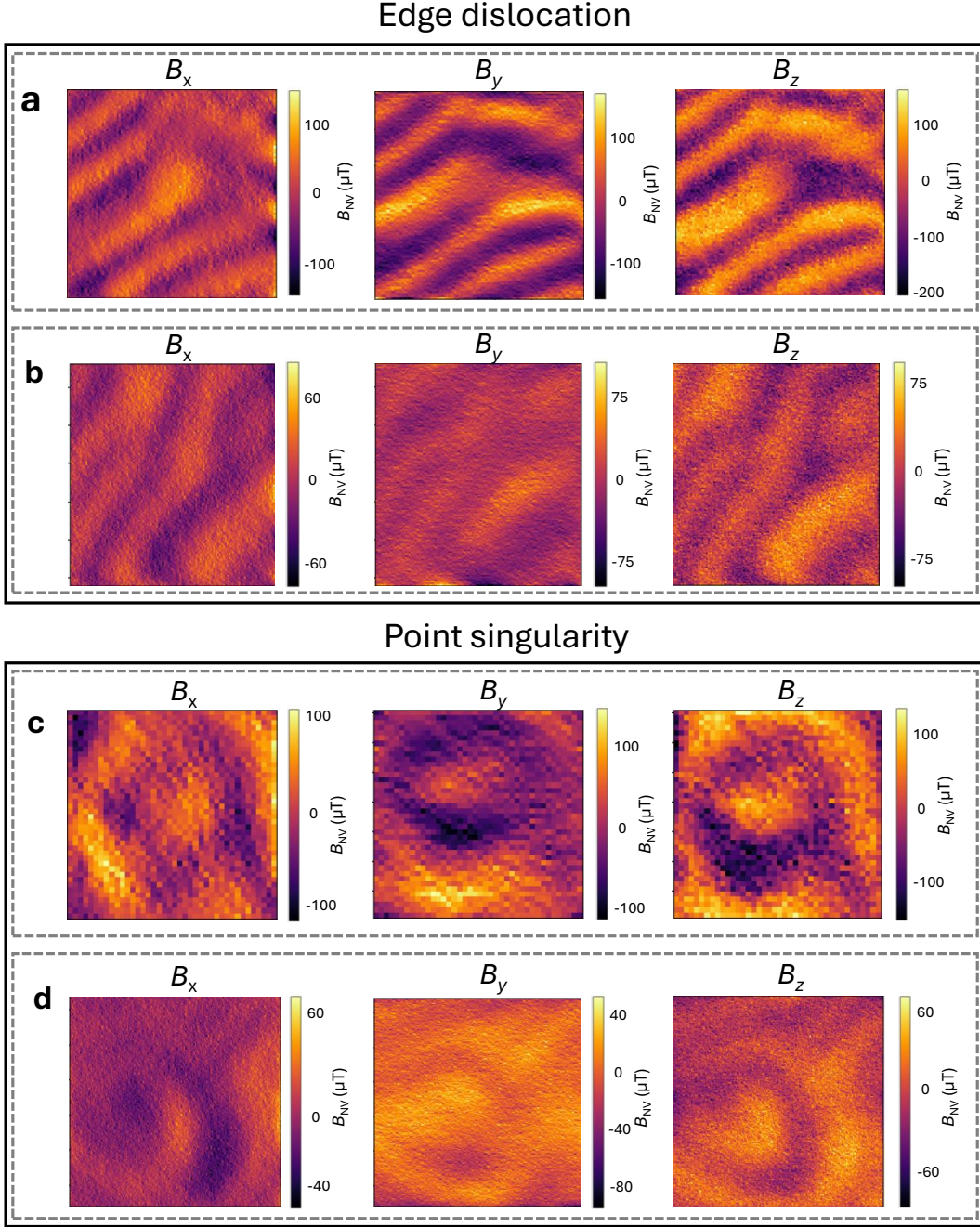


**Fig. S 11. Full- $B$  reconstruction around topological defects:** (a-b)  $x$ ,  $y$  and  $z$  components of the stray magnetic field reconstructed around two edge dislocations. Vector  $B$ -map for panel (a) has been shown in the Fig. 3a of the main text. The vector map for other one has been shown in the Supplementary Fig. S12a. (c-d)  $x$ ,  $y$  and  $z$  components of the stray magnetic field reconstructed around two isolated spots. Vector  $B$ -map for panel (c) has been shown in the Fig. 3b of the main text. The vector map for other one has been shown in the Supplementary Fig. S12b.

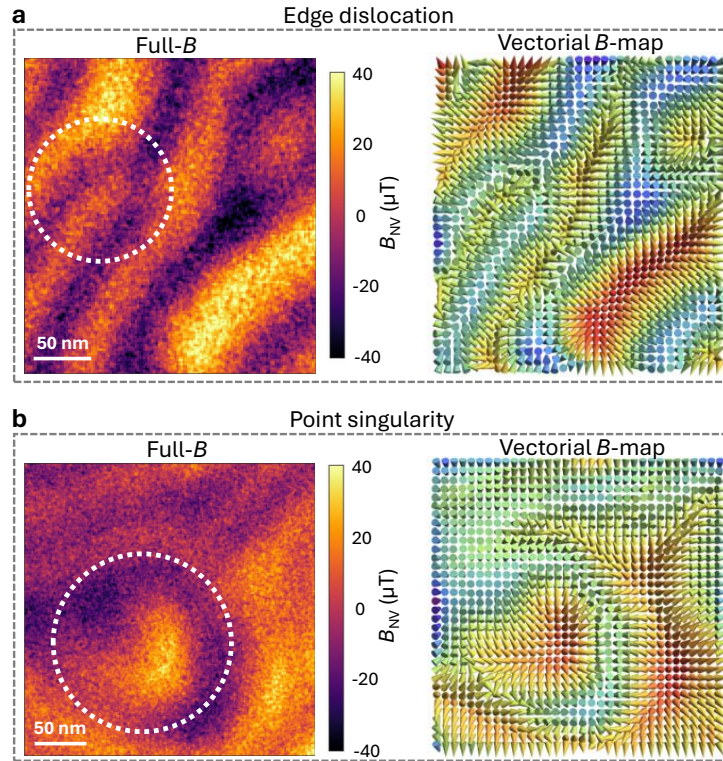


**Fig. S 12. Additional  $B$  field vector maps near an edge dislocation and point singularity:** For reproducibility, we have mapped vector  $B$ -maps on another point like singularity and an edge dislocation. Left panel of (a) shows a Full- $B$  image taken around another edge dislocation indicated with a white dotted circle. The corresponding vector map of the  $B$ -field has been shown in the right panel. (b) (Left panel) Full- $B$  image taken around a point singularity shown with a white dotted circle. The corresponding vector map of the  $B$ -field has been shown in the right panel.

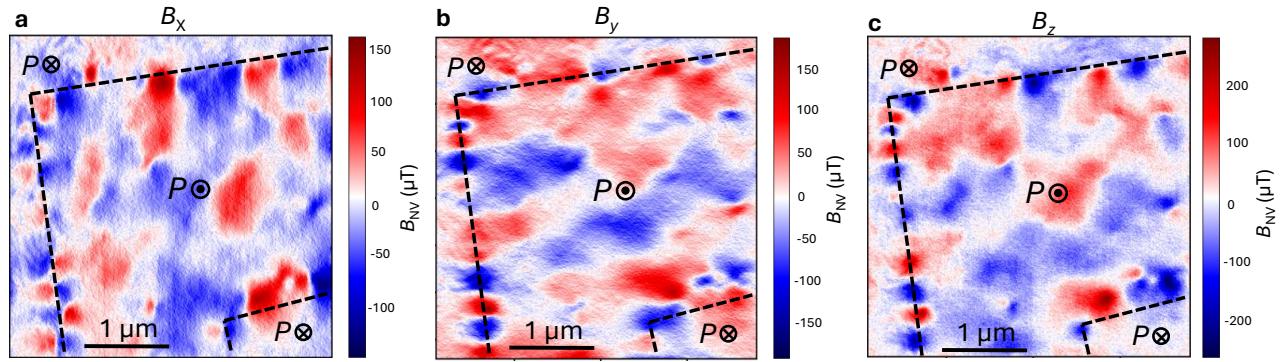


**Fig. S 13. Full- $B$  reconstruction in upward poled region shown in the Fig. 4(e) of the main text:** (a-c)  $x$ ,  $y$  and  $z$  components of the stray magnetic field reconstructed in the upward poled region shown in the Fig. 4e of the main text.

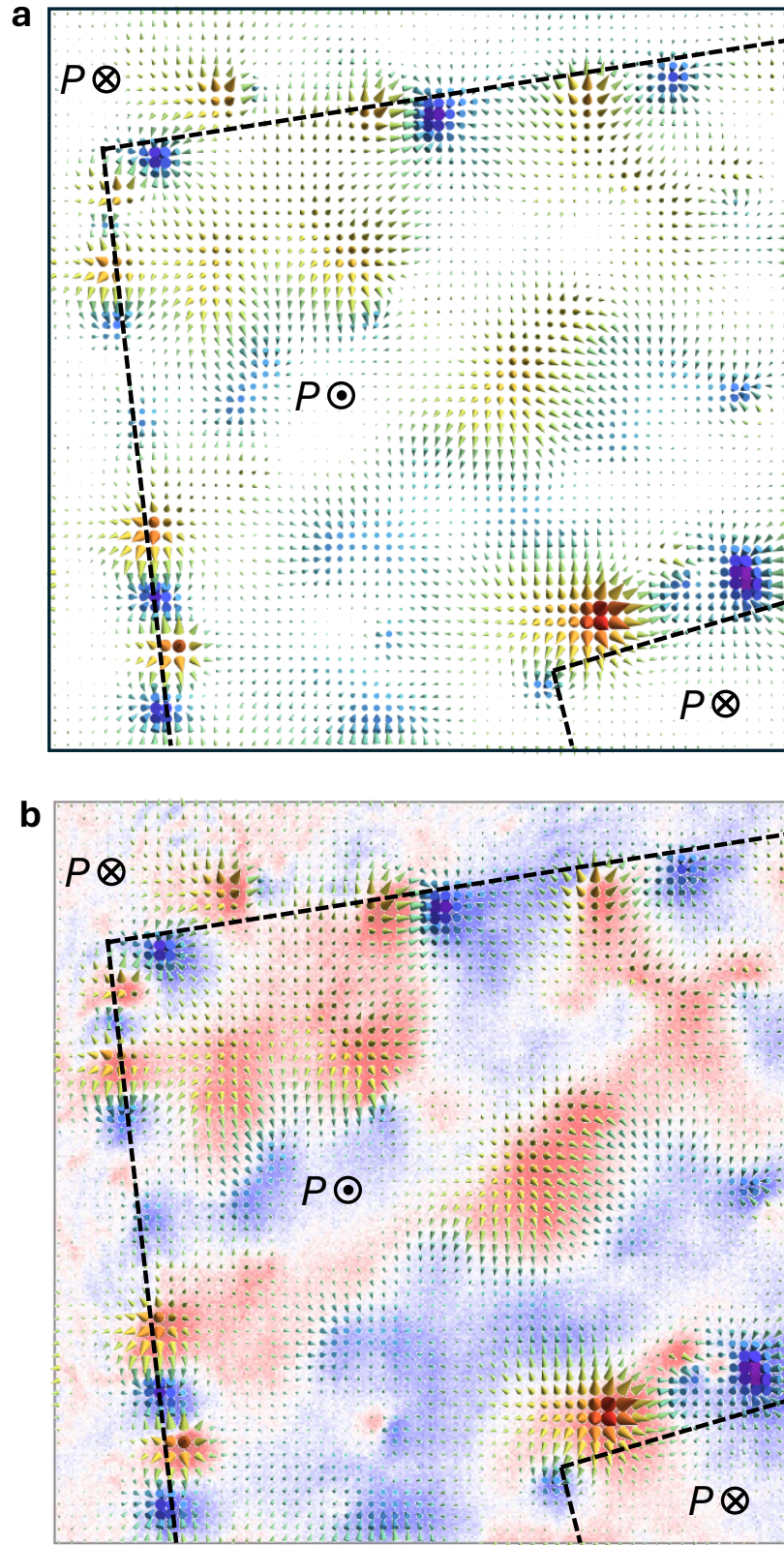


**Fig. S 14.** (a) Un-normalized vector map of  $B$  field in the upward poled region shown in the Fig. 4f of the main text. Panel (b) shows the same image overlaid on the full- $B$  image.

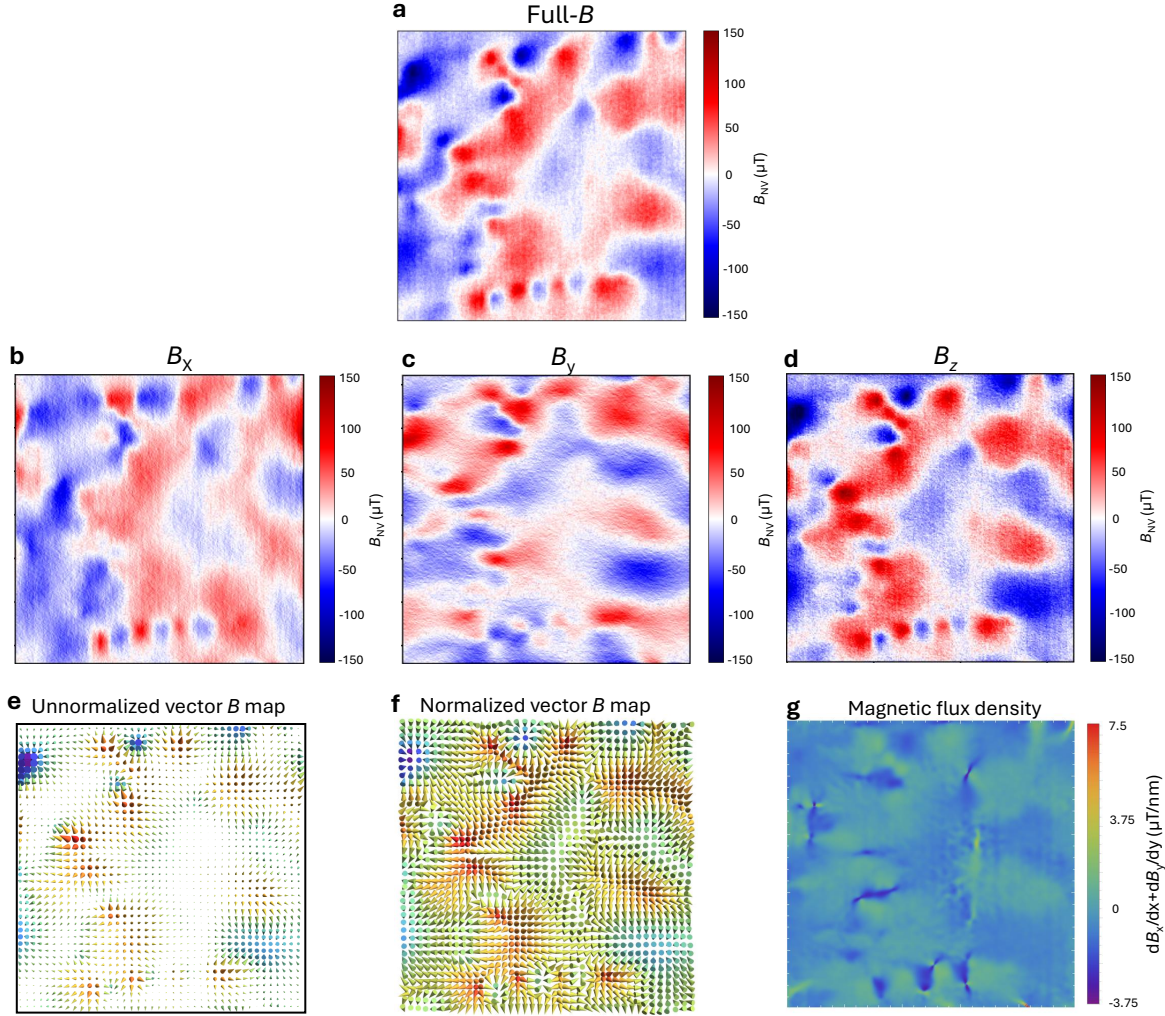


**Fig. S 15. Full- $B$  reconstruction in upward poled region on another sample:** For reproducibility, we have carried out Full- $B$  reconstruction in upward poled region on another sample. Panel (a) shows Full- $B$  image taken on another 1000 nm thick (111) oriented  $\text{BiFeO}_3$  film. panels (b), (c) and (d) correspond to  $x$ ,  $y$  and  $z$  component of stray magnetic field. (e) Vector  $B$  map constructed by plotting the linear combination of  $x$ ,  $y$  and  $z$  components at each pixel. To demonstrate the local orientation of  $B$  field more clearly, panel (f) shows the same plot after normalizing each vector. (g) Magnetic flux density obtained from the plot shown in the panel (e).

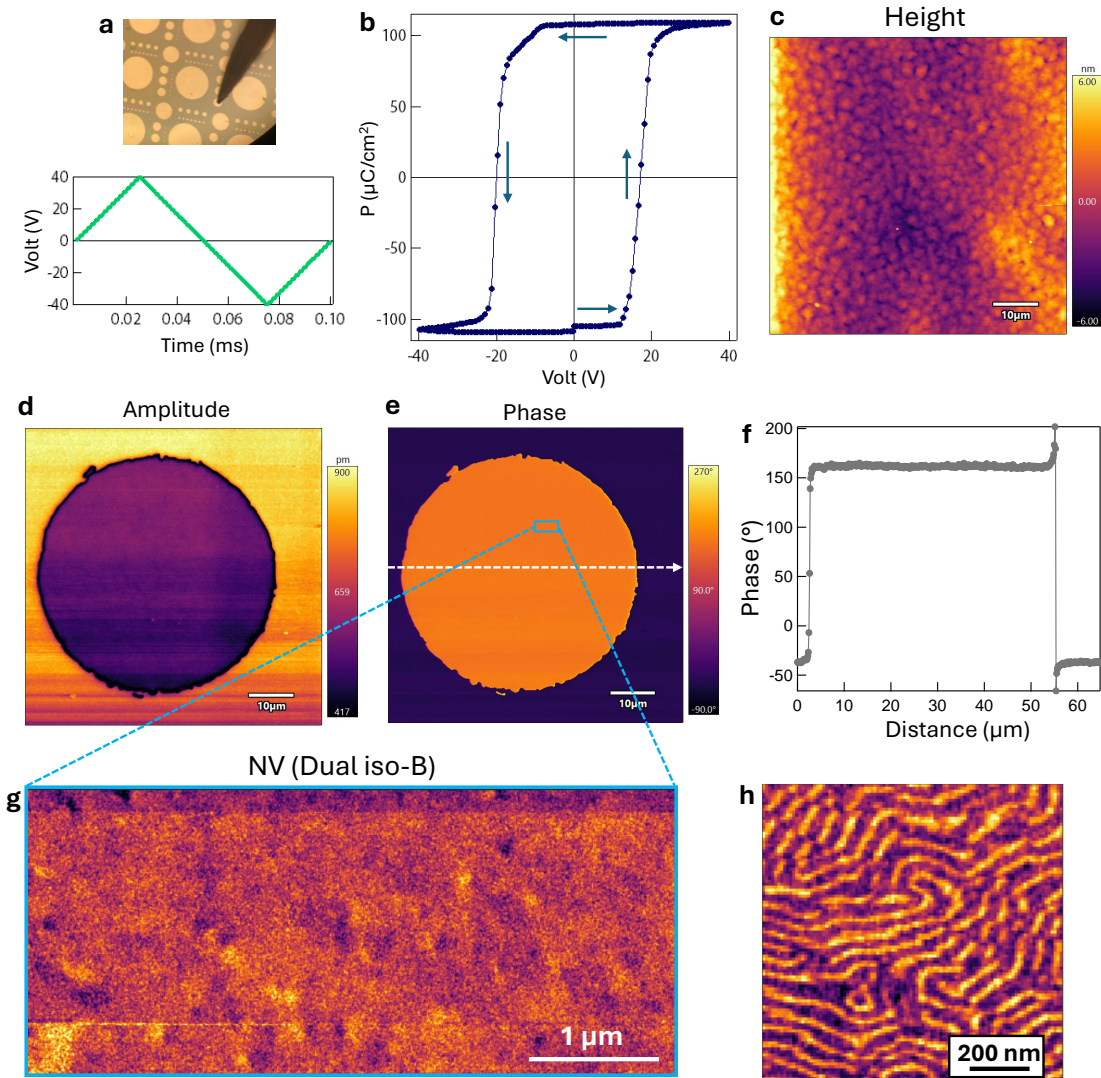


**Fig. S 16. NV image taken on region switched under top electrode:** (a) (top panel) Optical image of the top electrode used to switch the  $\mathbf{P}$  along  $[111]$ . Black arrow like region is the electrical probe through which voltage was applied. For this experiment, gold electrode was used as it could be easily dissolved. This is required as the presence of electrode drastically reduces the NV signal from sample due to an increase in effective flying distance of  $\text{NV}^-$  center. (bottom panel) Voltage ramping protocol utilized to switch the polarization. Panel (b) shows the corresponding evolution of the polarization during this voltage ramping protocol. At the final stage, the remnant polarization is out of the plane i.e. along the  $[111]$  direction. After switching, gold electrodes were dissolved in potassium iodide solution (Methods). Height profile of the surface after dissolving gold electrodes is shown in the panel (c). As evident pristine surface of  $\text{BiFeO}_3$  is fully recovered thus allowing for NV measurements. Panels (d) and (e) show the PFM amplitude and phase respectively taken on one the regions switched electrode. As evident, region under electrode is completely switched and homogeneous over large scales. A phase change of  $180^\circ$  warrants a complete switching of polarization from  $[\bar{1}\bar{1}\bar{1}]$  to  $[111]$ . Panel (g) shows the dual iso- $B$  image taken over 5 microns. As evident, the sample exhibits a homogeneous texture consistent with the results obtained on region switched with a conductive AFM tip. Please note that the outside regions still have glassy labyrinthine pattern (panel (h)) as discussed in the main text.

## SUPPLEMENTARY INFORMATION TEXT

### S1. CALIBRATING THE ORIENTATION OF NV<sup>-</sup> CENTER

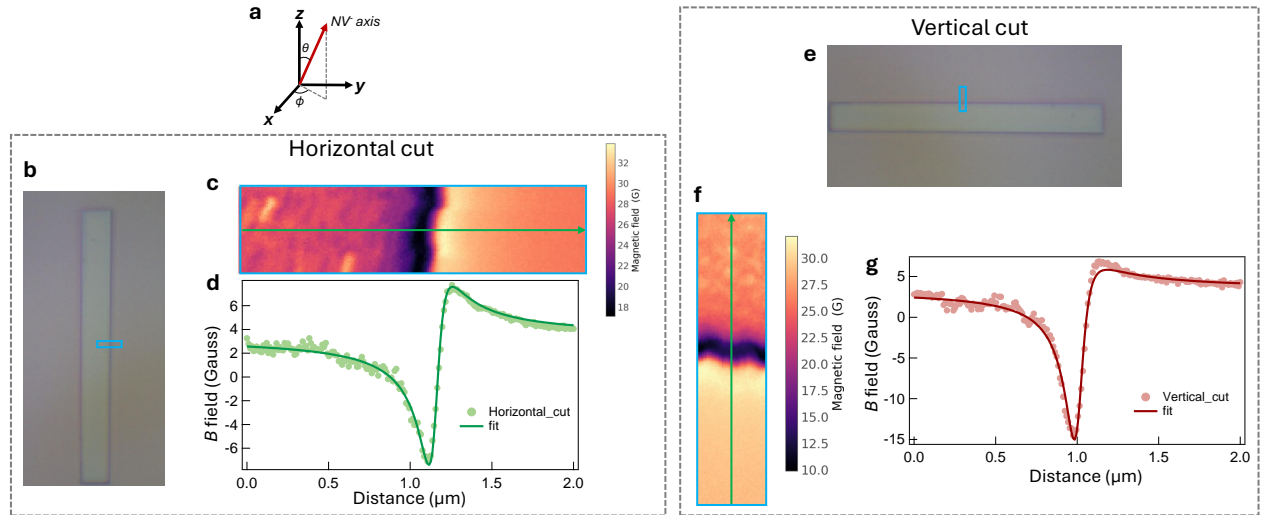


**Fig. S 17.** (a) Orientation of the NV<sup>-</sup> center in the laboratory frame of reference. (b) An optical image of a Ta(2 nm)/MgO/CoFeB(0.9 nm)/Ta(5 nm) sample with perpendicular magnetic anisotropy. Sky blue box shows the region where horizontal cuts of the magnetic profile across the edge of the sample was obtained. Full- $B$  scan of the same region is shown in the panel (c). (d) Line profile of the  $B$  field (averaged over 50 linescans) across the edge. Solid green line shows the fitting of experimental data with a model described in the reference [5]. (e-g) Similar set of data obtained in another orientation (rotated 90 ° with respect to the image in panel (b)).

To make any quantitative estimations, it is essential to first calibrate the orientation of the NV<sup>-</sup> center relative to the laboratory reference frame. The NV<sup>-</sup> center in diamond aligns along the one of four equivalent  $\langle 111 \rangle$  crystallographic directions, which would theoretically correspond to a polar angle ( $\theta$ ) of approximately 54.7 °. To determine this, we followed the procedure outlined in previous studies [5, 6], where the magnetic field profile is recorded across the edge of a known ferromagnetic sample Ta(2 nm)/MgO/CoFeB(0.9 nm)/Ta(5 nm) with perpendicular magnetic anisotropy. By measuring the  $B$ -field across edges of the sample in two different orientations of the sample and fitting the data to the analytical expressions provided in the reference [5], we determined the  $\theta$  to be 52 ° and the  $\phi$  to be 24 °. These angles were then used to decompose

the measured  $B$ -field, which is parallel to the  $NV^-$  center, into its components along the  $x$ ,  $y$ , and  $z$  axes in the laboratory frame, allowing us to construct vector maps of the magnetic field.

## S2. ORIGIN OF STRAY $B$ FIELD ON (111) SURFACE OF BIFEO<sub>3</sub>

The full cycloidal magnetization profile has three-dimensional texture; however, we can decompose this into two distinct contributions: the spiral-like texture of the spins (which lies in the plane defined by the polarization  $\vec{P}$  and the cycloid propagation direction  $\vec{k}$ ), and the spin density wave formed by the canted moments of these spins, which lies in the plane perpendicular to  $\vec{P}$  (see Fig. S18). For clarity, we will refer to the former as the “spiral” contribution to avoid confusion with the net cycloidal texture.

In (001) BiFeO<sub>3</sub>, the spiral contribution is near-zero because adjacent lattice sites at the surface layer (and each layer below) have oppositely-directed spins, resulting in almost no net surface magnetization (PHYSICAL REVIEW LETTERS 128, 187201 (2022)). However, the spin density wave is not cancelled and yields a net stray field.

In (111) BiFeO<sub>3</sub>, this is not the case. If we define a coordinate system where  $z$  is parallel to  $\vec{P}$  and  $x$  is parallel to  $\vec{k}$ , we can write the following for the SDW:

$$\vec{M}_{SDW} = A \cos(\vec{k} \cdot \vec{r})(\vec{e}_y) \quad (1)$$

$$= A \cos(|k|x)(\vec{e}_y) \quad (2)$$

In reciprocal space, this yields:

$$\tilde{M}_x(q) = 0 \quad (3)$$

$$\tilde{M}_y(q) = A\delta(q_y) \left( \delta(q_x - k) + \delta(q_x + k) \right) \quad (4)$$

$$\tilde{M}_z(q) = 0 \quad (5)$$

Combined with the Fourier-domain approach (PHYSICAL REVIEW APPLIED 14, 024076

(2020)) to calculating the stray field:

$$\begin{pmatrix} \tilde{B}_x \\ \tilde{B}_y \\ \tilde{B}_z \end{pmatrix} = -\frac{\mu_0}{2} e^{qz} \begin{pmatrix} q_x^2/q & q_x q_y/q & i q_x \\ q_x q_y/q & q_y^2/q & i q_y \\ i q_x & i q_y & -q \end{pmatrix} \begin{pmatrix} \tilde{M}_x \\ \tilde{M}_y \\ \tilde{M}_z \end{pmatrix} \quad (6)$$

this yields  $\vec{B} = 0$  for the SDW component.

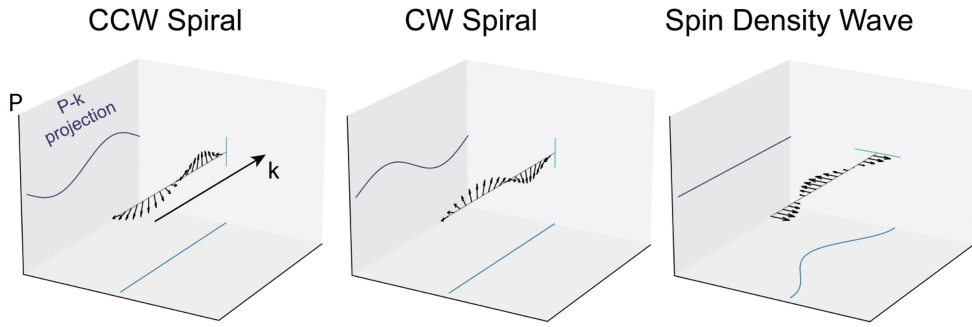


**Fig. S 18.** Three different components of the cycloid magnetization. CCW and CW denote counterclockwise and clockwise spiral respectively.

We can also calculate the stray field generated by the spiral ordering from a single monolayer of spins using:

$$\vec{M}_{spiral} = m_{Fe} \begin{pmatrix} \cos(kx) \\ 0 \\ \pm \sin(kx) \end{pmatrix} \quad (7)$$

where we find that now the generated stray field is *not* zero. The  $\pm$  comes because now, unlike our SDW, the cycloid has a chirality (+ for clockwise and - for anticlockwise). We can plot the magnetization for a single iteration of the different configurations in Figure S18.

However, we must address the question of cancellation of these magnetic moments from the antiferromagnetic ordering. If we define the stray field generated by a monolayer of our [111] orientation as  $\vec{B}$ , then the layer below this contributes a stray field of  $\exp(-|k|a)\vec{B}$ , where  $|k|$

is the cycloid wavenumber and  $a$  is the layer spacing. This allows us to write the net observed field as:

$$\vec{B}_{net} = \vec{B} \sum_{n=0}^{\infty} (-1)^n \exp(-nka) \quad (8)$$

$$= \vec{B} \frac{1}{1 + \exp(-ka)} \quad (9)$$

which for  $k = \frac{2\pi}{65\text{nm}}$  and  $a = \sqrt{3} \times 0.395\text{nm}$  gives  $\vec{B}_{net} \approx 0.5\vec{B}$ .

Following the steps described earlier, one could also obtain the expression for B originating solely from a single spin spiral propagating in the x-direction as below.

$$B_x(r) = -\frac{\mu_0}{2} m_{Fe} k (\cos(kx) \pm \cos(kx)) \quad (10)$$

$$B_y(r) = 0 \quad (11)$$

$$B_z(r) = \frac{\mu_0}{2} m_{Fe} k (\sin(kx) \pm \sin(kx)) \quad (12)$$

There are two key observations from these set of expressions:

(a) Firstly, for the spin spiral propagation direction in x-direction, the y-component of the B field goes to zero. This is indeed observed in our full-B reconstruction of the cycloid region as shown with the green color box in the Fig. S19(b). As is evident, the y-component of the B field becomes vanishingly small where cycloid propagation is almost parallel to the x-direction. We note that the y-component of the B field is not exactly zero due to slight deviation in cycloid propagation direction from x-direction in the region marked with green box.

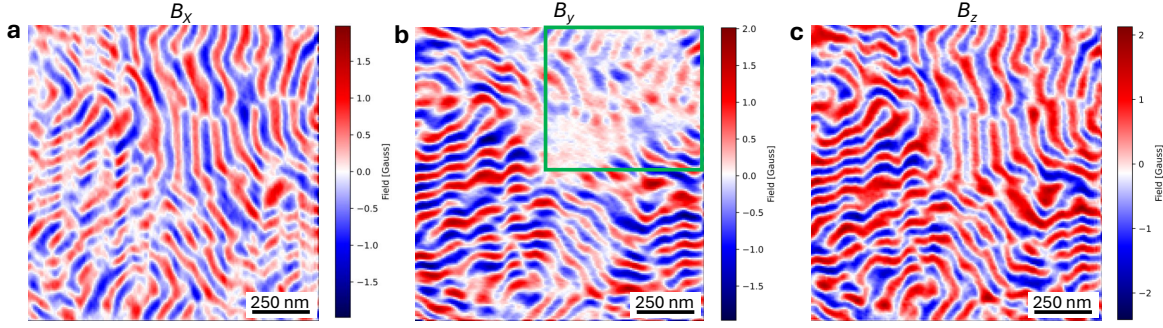


**Fig. S 19.** x, y and z components of the stray magnetic field reconstructed in the region shown in the panel (a) of Supplementary Fig. S9. Green box shows the region of interest where cycloid propagation is roughly along x-direction.

(b) Secondly, from these expressions, we can see that individually, the  $M_x$  and  $M_z$  components give rise to stray fields, but that these can either constructively or destructively interfere to yield different observed stray fields. For the destructive case (CCW chirality) all the components of the B field would go to zero. We have also made an order of magnitude estimation of the B field for both CCW and CW spirals and results are captured in the Fig. S20. For estimation, we assumed a NV flying distance of 60 nm (50 nm stand-off and 10 nm deep NV centers),  $k = 2\pi/65 \text{ nm}^{-1}$ . The spin only magnetic moment of Fe was assumed to be ( $\sqrt{35}\mu_B$  divided by the unit-cell cross section to get the areal density of a monolayer. A factor of 0.5 was assumed from the alternating layer structure (equation 9). As is evident, the estimated strength of B field for clockwise spiral has similar order of magnitude as observed in the experiments, however for the counter-clockwise the signal is exactly zero.

It is known from the previous scattering experiments (PHYSICAL REVIEW APPLIED 8, 014033 (2017)) on the same sample that the polarity of the cycloid switches from clockwise (+) to counter-clockwise (-) when the sample is poled upwards i.e. from

$$\cos(kx) \hat{\mathbf{x}} + \sin(kx) \hat{\mathbf{z}}$$

to

$$\cos(kx) \hat{x} - \sin(kx) \hat{z}$$

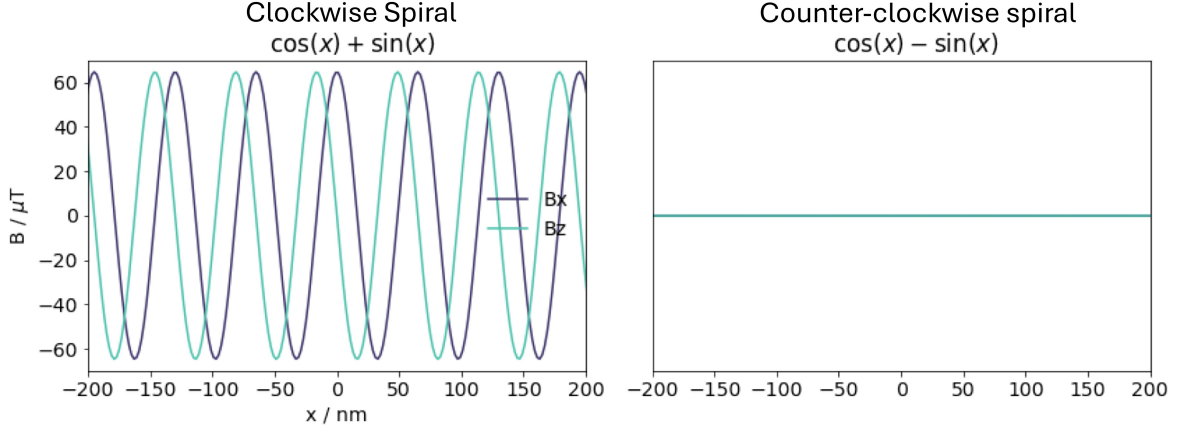


**Fig. S 20.** Computed stray magnetic fields for CW and CCW spirals.

In such a scenario, all the components of the B field go to zero. To verify this we have calculated the probability density of the modulus of B, across the upward switched regions and compared with the images with spin cycloids. The results are presented in Fig. S21. As is evident, the probability density plot for the switched upward region is centered on a lower  $|B|$  than the pristine regions. This means that the average magnitude of the stray B field in upward poled region is lower than the as-grown state which has cycloids. A similar analysis in the local regions (shown by boxes in Fig. S22) where B map is more homogeneous yields an even lower average B field than in the case of cycloids. For further validation, we have also recorded the full-B map in a region switched under a top electrode where the applied electric field is expected to be more homogeneous compared to the experiment with the metallized AFM tip. Since the presence of an electrode would significantly dampen the NV signal, the electrode was completely dissolved after switching with the FE tester similar to the one presented in the supplementary S14. Figs. S23 (a) and (b) show the full B map taken over the upward poled region along with

the probability density plot. As is evident, the magnitude of  $B$  is much smaller compared to the one with cycloids, emphasizing that the magnitude of the magnetization in the upward-poled region has reduced.

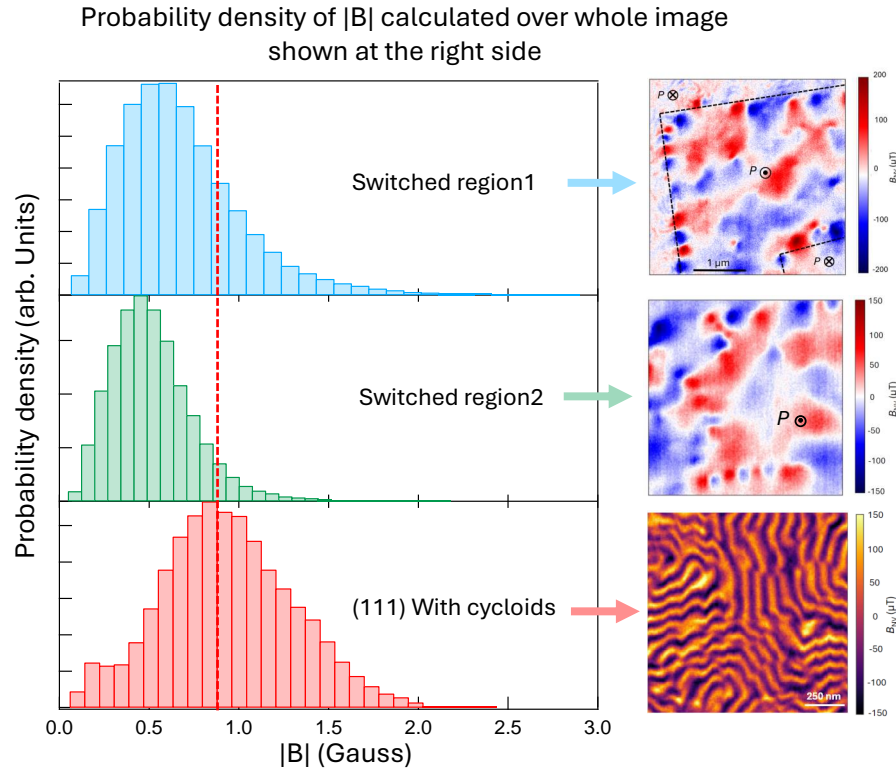


**Fig. S 21.** Probability density of  $|B|$  calculated over whole image shown at the right side.

We note that, such a situation has been discussed in the context of other systems as well (PHYSICAL REVIEW B 84,054404 (2011), Nano Lett. 18, 2263, 2018). In summary, we believe switching of cycloid polarity as an alternate interpretation apart from flexoelectric/flexomagnetic effects which could result in the formation of non-cycloidal homogeneous  $B$  field map observed in the upward switched region.

---

[1] Zhang, Q., Zhang, L., Jin, C., Wang, Y. & Lin, F. Calatom: A software for quantitatively analysing atomic columns in a transmission electron microscope image. *Ultramicroscopy* **202**, 114–120 (2019).

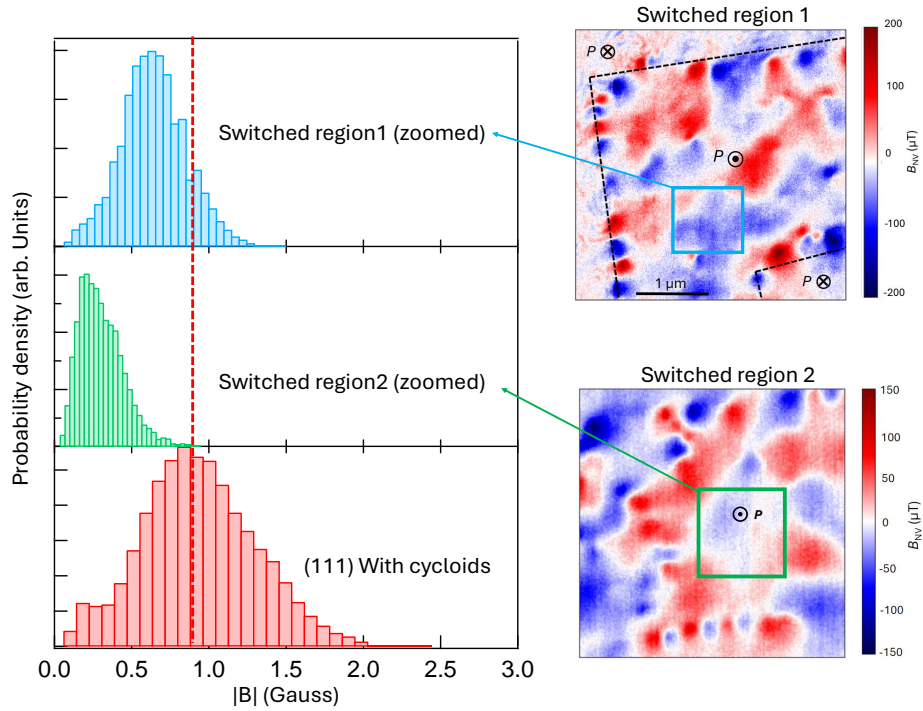


**Fig. S 22.** Probability density of  $|B|$  calculated over the square boxes shown at the right side.

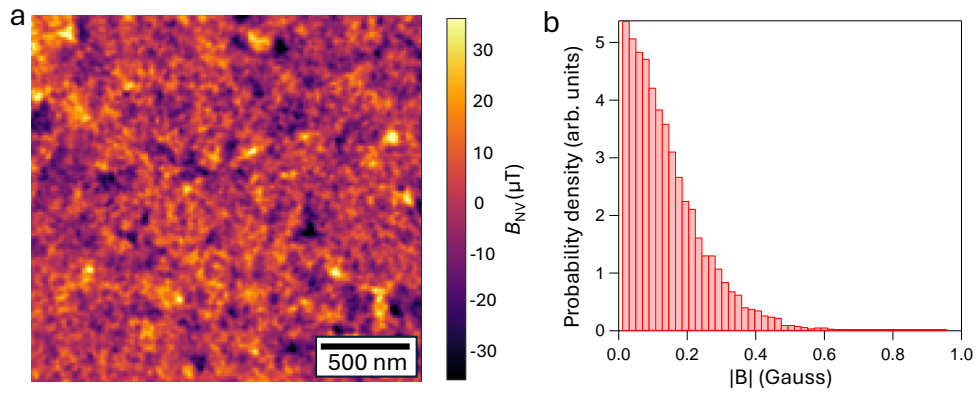


**Fig. S 23.** (a) Full-B image taken over the region which was switched upward under the electrode. (b) Probability density of  $|B|$  calculated over the image shown in the panel (a).

- [2] Dovzhenko, Y. *et al.* Magnetostatic twists in room-temperature skyrmions explored by nitrogen-vacancy center spin texture reconstruction. *Nature Communications* **9**, 2712 (2018). URL <https://doi.org/10.1038/s41467-018-05158-9>.
- [3] Broadway, D. *et al.* Improved current density and magnetization reconstruction through vector magnetic field measurements. *Phys. Rev. Appl.* **14**, 024076 (2020). URL <https://link.aps>.

[org/doi/10.1103/PhysRevApplied.14.024076](https://doi.org/10.1103/PhysRevApplied.14.024076).

- [4] Zhong, H. *et al.* Quantitative imaging of exotic antiferromagnetic spin cycloids in bifeo<sub>3</sub> thin films. *Phys. Rev. Appl.* **17**, 044051 (2022). URL <https://link.aps.org/doi/10.1103/PhysRevApplied.17.044051>.
- [5] Hingant, T. *et al.* Measuring the magnetic moment density in patterned ultrathin ferromagnets with submicrometer resolution. *Phys. Rev. Appl.* **4**, 014003 (2015). URL <https://link.aps.org/doi/10.1103/PhysRevApplied.4.014003>.
- [6] Meisenheimer, P. *et al.* Switching the spin cycloid in bifeo<sub>3</sub> with an electric field. *Nature Communications* **15**, 2903 (2024). URL <https://doi.org/10.1038/s41467-024-47232-5>.